



# Chemistry and Physics of a Low-metallicity Hot Core in the Large Magellanic Cloud

Takashi Shimonishi<sup>1,2</sup>, Ankan Das<sup>3</sup>, Nami Sakai<sup>4</sup>, Kei E. I. Tanaka<sup>5,6</sup>, Yuri Aikawa<sup>7</sup>, Takashi Onaka<sup>7,8</sup>, Yoshimasa Watanabe<sup>9</sup>, and Yuri Nishimura<sup>6,10</sup>

<sup>1</sup> Center for Transdisciplinary Research, Niigata University, Ikarashi-nincho 8050, Nishi-ku, Niigata, 950-2181, Japan; [shimonishi@env.sc.niigata-u.ac.jp](mailto:shimonishi@env.sc.niigata-u.ac.jp)

<sup>2</sup> Environmental Science Program, Department of Science, Faculty of Science, Niigata University, Ikarashi-nincho 8050, Nishi-ku, Niigata, 950-2181, Japan

<sup>3</sup> Indian Centre for Space Physics, 43 Chalandika, Garia Station Road, Kolkata 700084, India

<sup>4</sup> RIKEN, 2-1 Hirosawa, Wako, Saitama 351-0198, Japan

<sup>5</sup> Department of Earth and Space Science, Osaka University, Toyonaka, Osaka 560-0043, Japan

<sup>6</sup> ALMA Project, National Astronomical Observatory of Japan, Mitaka, Tokyo 181-8588, Japan

<sup>7</sup> Department of Astronomy, Graduate School of Science, The University of Tokyo, 7-3-1 Hongo, Bunkyo-ku, Tokyo 113-0033, Japan

<sup>8</sup> Department of Physics, Faculty of Science and Engineering, 2-1-1 Hodokubo, Hino, Tokyo 191-0042, Japan

<sup>9</sup> College of Engineering, Nihon University, 1 Nakagawara, Tokusada, Tamuramachi, Koriyama, Fukushima 963-8642, Japan

<sup>10</sup> Institute of Astronomy, The University of Tokyo, 2-21-1, Osawa, Mitaka, Tokyo 181-0015, Japan

Received 2019 December 2; revised 2020 January 14; accepted 2020 January 14; published 2020 March 16

## Abstract

We here present the results of 0.1 pc scale observations in 250 and 350 GHz toward a newly-discovered hot molecular core in a nearby low-metallicity galaxy, the Large Magellanic Cloud (LMC), with the Atacama Large Millimeter/submillimeter Array. A variety of C/N/O/Si/S-bearing molecules are detected toward the high-mass young stellar object, ST16. A rotating protostellar envelope is for the first time detected outside our Galaxy by SO<sub>2</sub> and <sup>34</sup>SO lines. An outflow cavity is traced by CCH and CN. The isotope abundance of sulfur in the source is estimated to be <sup>32</sup>S/<sup>34</sup>S = 17 and <sup>32</sup>S/<sup>33</sup>S = 53 based on SO, SO<sub>2</sub>, and CS isotopologues, suggesting that both <sup>34</sup>S and <sup>33</sup>S are overabundant in the LMC. Rotation diagram analyses show that the source is associated with hot gas (>100 K) traced by high-excitation lines of CH<sub>3</sub>OH and SO<sub>2</sub>, as well as warm gas (~50 K) traced by CH<sub>3</sub>OH, SO<sub>2</sub>, <sup>34</sup>SO, OCS, and CH<sub>3</sub>CN lines. A comparison of molecular abundances between LMC and Galactic hot cores suggests that organic molecules (e.g., CH<sub>3</sub>OH, a classical hot core tracer) show a large abundance variation in low metallicity, where the present source is classified into an organic-poor hot core. Our astrochemical simulations suggest that different grain temperatures during the initial ice-forming stage would contribute to the chemical differentiation. In contrast, SO<sub>2</sub> shows similar abundances within all of the known LMC hot cores, and the typical abundance roughly scales with the LMC's metallicity. Nitrogen-bearing molecules are generally less abundant in the LMC hot cores, except for NO. The present results suggest that chemical compositions of hot cores do not always simply scale with the metallicity.

*Unified Astronomy Thesaurus concepts:* Astrochemistry (75); Dust continuum emission (412); Interstellar molecules (849); Protostars (1302); Large Magellanic Cloud (903); Interstellar line emission (844); Isotopic abundances (867); Metallicity (1031); Star formation (1569); Submillimeter astronomy (1647)

## 1. Introduction

Understanding low-metallicity astrochemistry is crucial to unveiling chemical processes in the past universe, where the metallicity was significantly lower than the present-day galaxies. Observations of star-forming regions in nearby low-metallicity galaxies and comparative studies of their chemical compositions with Galactic counterparts play an important role for this purpose.

Hot molecular cores are one of the early stages of star formation, and they play a key role in the chemical processing of interstellar molecules, especially for complex molecular species. Physically, hot cores are defined as having a small source size ( $\leq 0.1$  pc), high density ( $\geq 10^6$  cm<sup>-3</sup>), and high gas/dust temperature ( $\geq 100$  K; e.g., van Dishoeck & Blake 1998; Kurtz et al. 2000; van der Tak 2004). Characteristic chemistry in hot cores starts from sublimation of ice mantles by stellar radiation and/or shock. This leads to the enrichment of gas-phase molecules, and parental species such as methanol (CH<sub>3</sub>OH) and ammonia (NH<sub>3</sub>) evolve into larger complex organic molecules (COMs) in warm and dense circumstellar environment (e.g., Nomura & Millar 2004; Garrod & Herbst 2006; Herbst & van Dishoeck 2009; Balucani et al. 2015). Grain surface chemistry also contributes to the

formation of COMs upon heating of ice mantles. Consequently, hot cores show rich spectral lines in the radio regime. Detailed studies of hot core chemistry are thus crucial to understand chemical processes triggered by star formation activities.

The Large Magellanic Cloud (LMC) is an excellent target to study interstellar/circumstellar chemistry at low metallicity, thanks to the proximity ( $49.97 \pm 1.11$  kpc, Pietrzyński et al. 2013) and the decreased metallicity environment ( $\sim 1/2$ – $1/3$  of the solar metallicity; e.g., Dufour et al. 1982; Westerlund 1990; Russell & Dopita 1992; Andrievsky et al. 2001; Rolleston et al. 2002). The low dust-to-gas ratio makes the interstellar radiation field less attenuated, and thus photoprocessing of interstellar medium could be more effective in the LMC than in our Galaxy. The environmental differences caused by the decreased metallicity would lead to a different chemical history of star- and planet-forming regions in the LMC and other low-metallicity galaxies. Hot core chemistry in the LMC should provide us with useful information to understand chemical complexity in the past metal-poor universe.

Chemical compositions of interstellar molecules in the LMC have been studied extensively. Molecular-cloud-scale chemistry ( $\lesssim 10$  pc) has been investigated by radio single-dish observations (e.g., Johansson et al. 1994; Chin et al. 1997;

Heikkilä et al. 1999; Wang et al. 2009; Paron et al. 2014, 2016; Nishimura et al. 2016; Tang et al. 2017). Interferometry observations in millimeter have probed distributions of dense molecular gas at a clump scale (a few pc; e.g., Wong et al. 2006; Seale et al. 2012; Anderson et al. 2014). The Atacama Large Millimeter/submillimeter Array (ALMA) has provided us with an unprecedented sensitivity and spatial resolution to study physical properties of dense molecular gas around young stellar objects (YSOs) at a subparsec scale (e.g., Indebetouw et al. 2013; Fukui et al. 2015; Saigo et al. 2017; Nayak et al. 2018). For solid-state molecules, compositions of ice mantles have been probed by infrared spectroscopic observations toward embedded YSOs (e.g., van Loon et al. 2005; Shimonishi et al. 2008, 2010, 2016a; Oliveira et al. 2009, 2011; Seale et al. 2011).

Chemistry of hot cores at low metallicity is now emerging with discoveries of extragalactic hot cores in the LMC with ALMA (Shimonishi et al. 2016b; Sewilo et al. 2018). The formation of organic molecules in low-metallicity environments is one of the important issues in recent astrochemical studies of low-metallicity star-forming regions. Shimonishi et al. (2016b) reported that organic molecules such as  $\text{CH}_3\text{OH}$ ,  $\text{H}_2\text{CO}$ , and  $\text{HNCO}$  toward a hot molecular core in the LMC (ST11) are underabundant by one to three orders of magnitude compared to Galactic hot cores. On the other hand, Sewilo et al. (2018) reported the detection of  $\text{CH}_3\text{OH}$  and even larger COMs toward other different hot molecular cores in the LMC (N113 A1 and B3). In contrast to the ST11 hot core, they found that the molecular abundances of COMs in the N113 hot cores are scaled by the metallicity of the LMC and comparable to those found at the lower end of the range in Galactic hot cores. Because of the limited number of current samples and the limited frequency coverage, chemical processes to form organic molecules in low-metallicity hot cores are still an open question. Besides those observational approaches, astrochemical simulations of low-metallicity hot core chemistry are presented in Bayet et al. (2008) and Acharyya & Herbst (2018). Observational efforts to identify and analyze further low-metallicity hot cores are important to constrain various uncertainties involved in astrochemical models.

In this paper, we report the results of high spatial resolution submillimeter observations with ALMA toward a high-mass YSO in the LMC, and present the discovery of a new hot molecular core. Section 2 describes the details of the target source, observations, and data reduction. The obtained molecular line spectra and images are described in Section 3. Derivation of physical quantities and molecular abundances from the present data is described in Section 4. Properties of the observed hot core and the comparison of the molecular abundances with those of other LMC and Galactic hot cores are discussed in Section 5, where astrochemical simulations of low-metallicity hot cores are also presented. Distributions of molecules in a rotating protostellar envelope and an outflow cavity, as well as isotope abundances of sulfur in the source, are also discussed in Section 5. The conclusions are given in Section 6.

## 2. Target, Observations, and Data Reduction

### 2.1. Target

The target of the present ALMA observations is an infrared source, IRAS 05195–6911 or ST16 (hereafter ST16), located

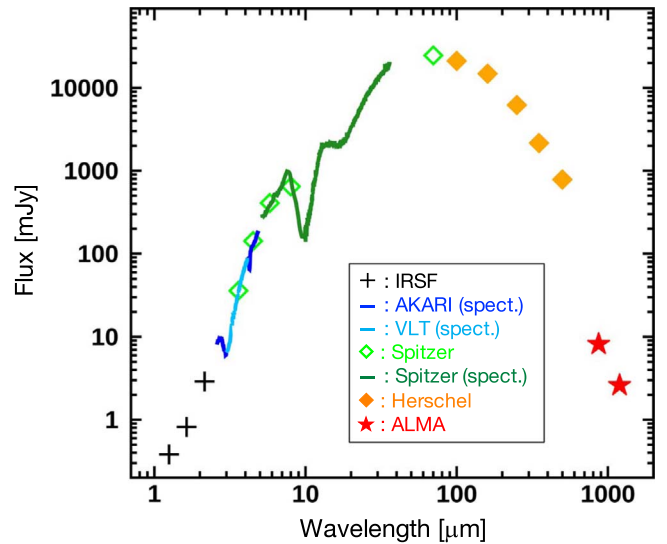


**Figure 1.** Spectral energy distribution of the observed high-mass young stellar object, ST16. The plotted data are based on IRSF/SIRIUS JHK<sub>s</sub> photometry (pluses, black; Kato et al. 2007), AKARI/IRC spectroscopy (solid line, blue; Shimonishi et al. 2010), VLT/ISAAC spectroscopy (solid line, light blue; Shimonishi et al. 2016a), *Spitzer*/IRAC and MIPS photometry (open diamonds, light green; Meixner et al. 2006), *Spitzer*/MIPS spectroscopy (solid line, green; Kemper et al. 2010), *Herschel*/PACS and SPIRE photometry (filled diamonds, orange; Meixner et al. 2013), and ALMA 870 and 1200  $\mu\text{m}$  continuum measurements obtained in this work (filled star, red).

near the N119 star-forming region in the LMC. Previous infrared spectroscopic studies have classified the source as an embedded high-mass YSO (Seale et al. 2009; Shimonishi et al. 2016a). A spectral energy distribution (SED) of the source is shown in Figure 1 (data are collected from available databases and literatures including Meixner et al. 2006, 2013; Kato et al. 2007; Kemper et al. 2010; Shimonishi et al. 2016a). The bolometric luminosity of the source is estimated to be  $3.1 \times 10^5 L_{\odot}$  by integrating the SED from 1 to 1200  $\mu\text{m}$ .

### 2.2. Observations

Observations were carried out with ALMA as a part of Cycle 4 (2016.1.00394.S) and Cycle 6 (2018.1.01366.S) programs (PI T. Shimonishi). A summary of the present observations is shown in Table 1. The target high-mass YSO is located at R.A. =  $05^{\text{h}}19^{\text{m}}12^{\text{s}}31$  and decl. =  $-69^{\circ}9'7''3$  (ICRS), based on the *Spitzer* SAGE infrared catalog (Meixner et al. 2006). The source's positional accuracy is about  $0''.3$ . The pointing center of antennas is R.A. =  $05^{\text{h}}19^{\text{m}}12^{\text{s}}30$  and decl. =  $-69^{\circ}9'6''.8$  (ICRS), which roughly corresponds to the infrared center of the target.

The total on-source integration time is 16.1 minutes for Band 6 data and 35.8 minutes for Band 7. Flux, bandpass, and phase calibrators are J0519–4546, J0635–7516, and J0526–6749 for Band 6, while J0519–4546, J0519–4546, and J0529–7245 for Band 7, respectively. Four spectral windows are used to cover the sky frequencies of 241.25–243.12, 243.61–245.48, 256.75–258.62, and 258.60–260.48 GHz for Band 6 and 336.97–338.84, 338.77–340.64, 348.85–350.72, and 350.65–352.53 GHz for Band 7. The channel spacing is 0.98 MHz, which corresponds to  $1.2 \text{ km s}^{-1}$  for Band 6 and  $0.85 \text{ km s}^{-1}$  for Band 7. The total number of antennas is 44 for Band 6 and 46 for Band 7. The minimum–maximum baseline lengths are 15.1–704.1 m for Band 6 and 15.1–783.5 m for Band 7.

**Table 1**  
Observation Summary

	Observation Date	On-source Time (minutes)	Mean PWV <sup>a</sup> (mm)	Number of Antennas	Baseline		Beam size <sup>b</sup> (" × ")	MRS <sup>c</sup> (")	Channel Spacing
					Min (m)	Max (m)			
Band 6 (250 GHz)	2016 Nov 30 (Cycle 4)	16.1	1.9–2.5	44	15.1	704.1	0.54 × 0.40	3.6	0.98 MHz (1.2 km s <sup>-1</sup> )
Band 7 (350 GHz)	2018 Dec 4 (Cycle 6)	35.8	0.5–0.6	46	15.1	783.5	0.37 × 0.32	3.3	0.98 MHz (0.85 km s <sup>-1</sup> )
						(C40-4)			
						(C43-4)			

**Notes.**

<sup>a</sup> Precipitable water vapor.

<sup>b</sup> The average beam size achieved by TCLEAN with the Briggs weighting and the robustness parameter of 0.5. Note that we use a common circular restoring beam size of 0".40 for Band 6 and 7 data to construct the final images.

<sup>c</sup> Maximum Recoverable Scale.

A full-width at half-maximum (FWHM) of the primary beam is about 25" for Band 6 and 18" for Band 7.

### 2.3. Data Reduction

Raw data are processed with the Common Astronomy Software Applications (CASA) package. For calibration, CASA 4.7.2 is used for Band 6 and CASA 5.4.0 is used for Band 7. For imaging, we use CASA 5.4.0 for all data. With the Briggs weighting and the robustness parameter of 0.5, the synthesized beam sizes of 0".52–0".56 × 0".39–0".41 with a position angle of  $-23^\circ$  for Band 6 and 0".36–0".38 × 0".31–0".32 with a position angle of  $-17^\circ$  for Band 7 are achieved. In this paper, we have used a common circular restoring beam size of 0".40 for Band 6 and 7 data, in order to accommodate the spectral analyses in separated frequency regions. This beam size corresponds to 0.097 pc at the distance of the LMC. The continuum image is constructed by selecting line-free channels from the four spectral windows. After the clean process, the images are corrected for the primary beam pattern using the *impbcor* task in CASA. The self-calibration is not applied.

The spectra and continuum flux are extracted from the 0".42 (0.10 pc) diameter circular region centered at R.A. = 05<sup>h</sup>19<sup>m</sup>12<sup>s</sup>.295 and decl. =  $-69^\circ 9' 7''.34$  (ICRS), which corresponds to the 870  $\mu$ m continuum center of ST16. The continuum emission is subtracted from the spectral data using the *uvcontsub* task in CASA before the spectral extraction.

## 3. Results

### 3.1. Spectra

Figure 2 shows molecular emission line spectra extracted from the position of ST16. Spectral lines are identified with the aid of the Cologne Database for Molecular Spectroscopy<sup>11</sup> (CDMS; Müller et al. 2001, 2005) and the molecular database of the Jet Propulsion Laboratory<sup>12</sup> (JPL; Pickett et al. 1998). The detection criteria adopted here are the  $2.5\sigma$  significance level and the velocity coincidence with the systemic velocity of nearby CO clouds (between 260 and 270 km s<sup>-1</sup>, estimated using the MAGMA data presented in Wong et al. 2011).

Molecular emission lines of CH<sub>3</sub>OH, H<sub>2</sub>CO, CCH, H<sup>13</sup>CO<sup>+</sup>, CS, C<sup>34</sup>S, C<sup>33</sup>S, SO, <sup>34</sup>SO, <sup>33</sup>SO, SO<sub>2</sub>, <sup>34</sup>SO<sub>2</sub>, <sup>33</sup>SO<sub>2</sub>, OCS,

H<sub>2</sub>CS, CN, NO, HNCO, H<sup>13</sup>CN, CH<sub>3</sub>CN, and SiO are detected from the observed region. Multiple high excitation lines (upper state energy >100 K) are detected for CH<sub>3</sub>OH, SO<sub>2</sub>, <sup>34</sup>SO<sub>2</sub>, <sup>33</sup>SO<sub>2</sub>, OCS, and CH<sub>3</sub>CN. Complex organic molecules larger than CH<sub>3</sub>OH are not detected. In total, we have detected 90 transitions, out of which, 30 lines are due to CH<sub>3</sub>OH, and 27 lines are due to SO<sub>2</sub> and its isotopologues. Radio recombination lines are not detected, though moderately intense lines such as H36 $\beta$  (260.03278 GHz) or H41 $\gamma$  (257.63549 GHz) are covered in the observed frequency range.

Line parameters are measured by fitting a Gaussian profile to observed lines. Based on the fitting, we estimate the peak brightness temperature, the FWHM, the LSR velocity, and the integrated intensity for each line. Measured line widths are typically 3–6 km s<sup>-1</sup>. Full details of the line fitting can be found in Appendix A (tables of measured line parameters) and Appendix B (figures of fitted spectra). The tables also contain estimated upper limits on important non-detection lines.

### 3.2. Images

Figures 3 and 4 shows synthesized images of continuum and molecular emission lines observed toward the target region. The molecular line images are constructed by integrating spectral data in the velocity range where the emission is seen. For CH<sub>3</sub>OH and SO<sub>2</sub>, high-excitation line images ( $E_u > 100$  K for CH<sub>3</sub>OH and  $>80$  K for SO<sub>2</sub>) and low-excitation line images ( $E_u < 50$  K for CH<sub>3</sub>OH and 36 K for SO<sub>2</sub>) are separately constructed, because these molecules show two different temperature components in their rotation diagrams (see Section 4.1).

The continuum emission, as well as most of molecular emission lines except for CCH and CN, are centered at the position of the high-mass YSO. SO, NO, and low- $E_u$  SO<sub>2</sub> show a secondary peak at the east side of the YSO. The distributions of continuum, CS, SO, H<sub>2</sub>CO, CCH, CN, and possibly H<sup>13</sup>CO<sup>+</sup> are elongated in the north–south direction.

We have estimated the spatial extent of each emission around the YSO by fitting a two-dimensional Gaussian to the peak position. Compact distributions, i.e., FWHM = 0".38–0".46 (0.09–0.11 pc) that is comparable with the beam size, are seen in high- $E_u$  CH<sub>3</sub>OH, low- and high- $E_u$  SO<sub>2</sub>, <sup>34</sup>SO<sub>2</sub>, <sup>33</sup>SO<sub>2</sub>, OCS, <sup>34</sup>SO, <sup>33</sup>SO, CH<sub>3</sub>CN, and HNCO. Slightly extended distributions, i.e., FWHM = 0".52–0".76 (0.13–0.18 pc), are seen in H<sub>2</sub>CO, low- $E_u$  CH<sub>3</sub>OH, SO, C<sup>34</sup>S, C<sup>33</sup>S, H<sub>2</sub>CS, NO, H<sup>13</sup>CN, SiO, and continuum. Among them, the distributions of

<sup>11</sup> <https://cdms.astro.uni-koeln.de/classic/>

<sup>12</sup> <http://spec.jpl.nasa.gov>



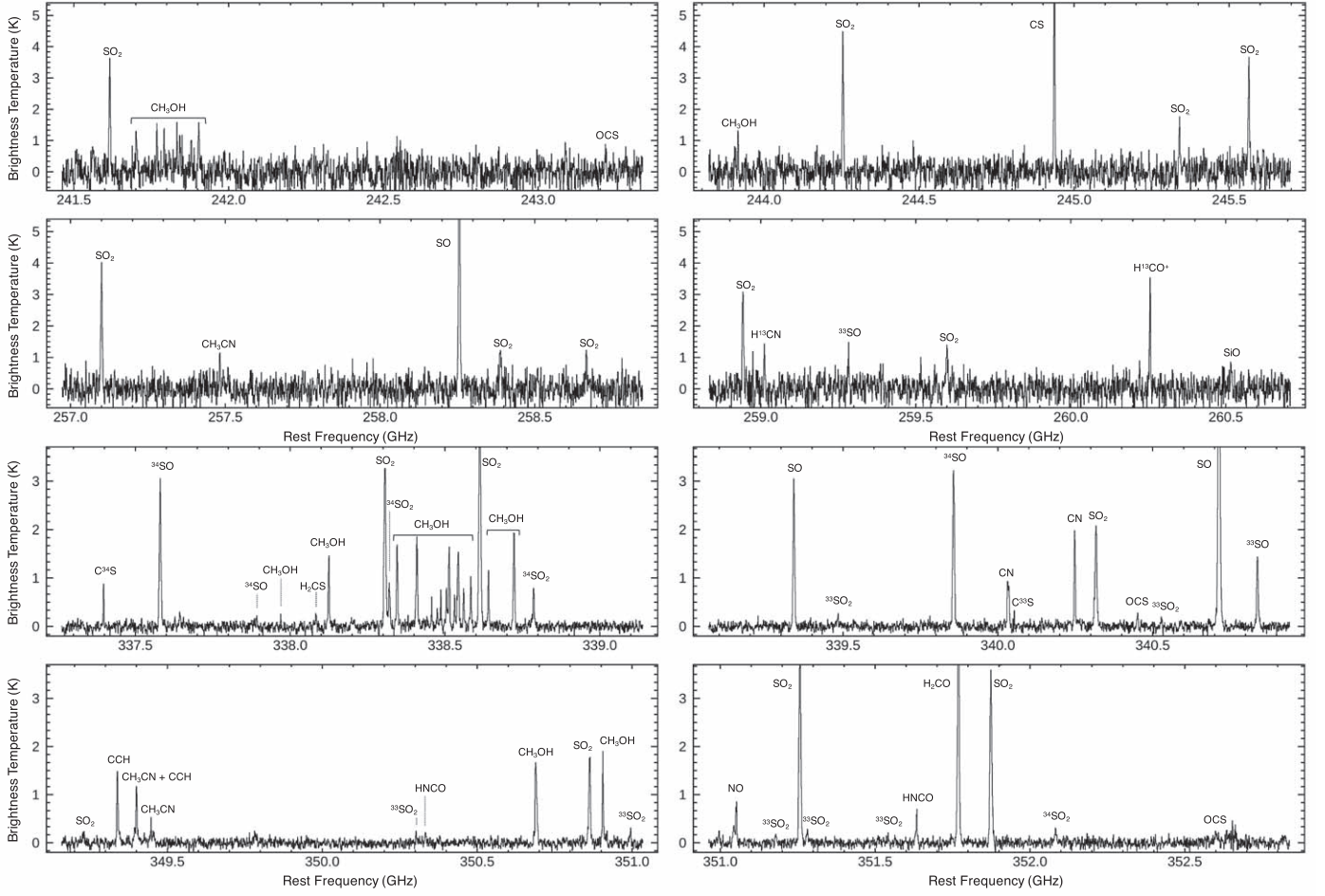


**Figure 2.** ALMA Band 6 and 7 spectra of ST16 extracted from a  $0.42$  ( $0.10$  pc) diameter region centered at the continuum and molecular emission peak. Detected emission lines are labeled. The source velocity of  $264.5 \text{ km s}^{-1}$  is assumed.

$\text{H}^{13}\text{CN}$  and  $\text{H}_2\text{CS}$ , and possibly  $\text{C}^{34}\text{S}$ ,  $\text{C}^{33}\text{S}$ , and  $\text{SiO}$ , are marginally off the continuum center. The  $\text{NO}$  distribution seems to be patchy. The continuum emission has a sharp peak around the YSO position but is also widely distributed within the observed field, as shown by the  $5\sigma$  contour in Figure 3. Similar characteristics (sharp peak and extended plateau) are also seen for  $\text{SO}$  and  $\text{H}_2\text{CO}$ . Clearly extended distributions, i.e.,  $\text{FWHM} = 1''\text{--}2''$  ( $0.24\text{--}0.49$  pc), are seen in  $\text{CS}$ ,  $\text{CCH}$ ,  $\text{CN}$ , and  $\text{H}^{13}\text{CO}^+$ . The distributions of  $\text{CCH}$  and  $\text{CN}$  are significantly different from those of other molecules and will be further discussed in Section 5.7.

## 4. Analysis

### 4.1. Rotation Diagram Analyses

Column densities and rotation temperatures of  $\text{CH}_3\text{OH}$ ,  $\text{SO}_2$ ,  $^{34}\text{SO}_2$ ,  $^{33}\text{SO}_2$ ,  $\text{SO}$ ,  $^{34}\text{SO}$ ,  $\text{OCS}$ , and  $\text{CH}_3\text{CN}$  are estimated with the aid of the rotation diagram analysis, because multiple lines with different excitation energies are detected (Figure 5). We here assume an optically thin condition and the local thermodynamic equilibrium (LTE). The assumption of optically thin emission is mostly valid for the present source (see discussion in Sections 5.2, 5.5, and 5.7). We use the following formulae based on the standard treatment of the rotation

diagram analysis (e.g., Sutton et al. 1995; Goldsmith & Langer 1999):

$$\log\left(\frac{N_u}{g_u}\right) = -\left(\frac{\log e}{T_{\text{rot}}}\right)\left(\frac{E_u}{k}\right) + \log\left(\frac{N}{Q(T_{\text{rot}})}\right), \quad (1)$$

where

$$\frac{N_u}{g_u} = \frac{3k \int T_b dV}{8\pi^3 \nu S \mu^2}, \quad (2)$$

and  $N_u$  is a column density of molecules in the upper energy level,  $g_u$  is the degeneracy of the upper level,  $k$  is the Boltzmann constant,  $\int T_b dV$  is the integrated intensity estimated from the observations,  $\nu$  is the transition frequency,  $S$  is the line strength,  $\mu$  is the dipole moment,  $T_{\text{rot}}$  is the rotational temperature,  $E_u$  is the upper state energy,  $N$  is the total column density, and  $Q(T_{\text{rot}})$  is the partition function at  $T_{\text{rot}}$ . All of the spectroscopic parameters required in the analysis are extracted from the CDMS database.

For  $\text{CH}_3\text{OH}$  and  $\text{SO}_2$ , a straight-line fit is separated into two temperature regimes, because different temperature components are clearly seen in the diagram. We use the transitions with  $E_u < 100$  K to fit the lower-temperature component and

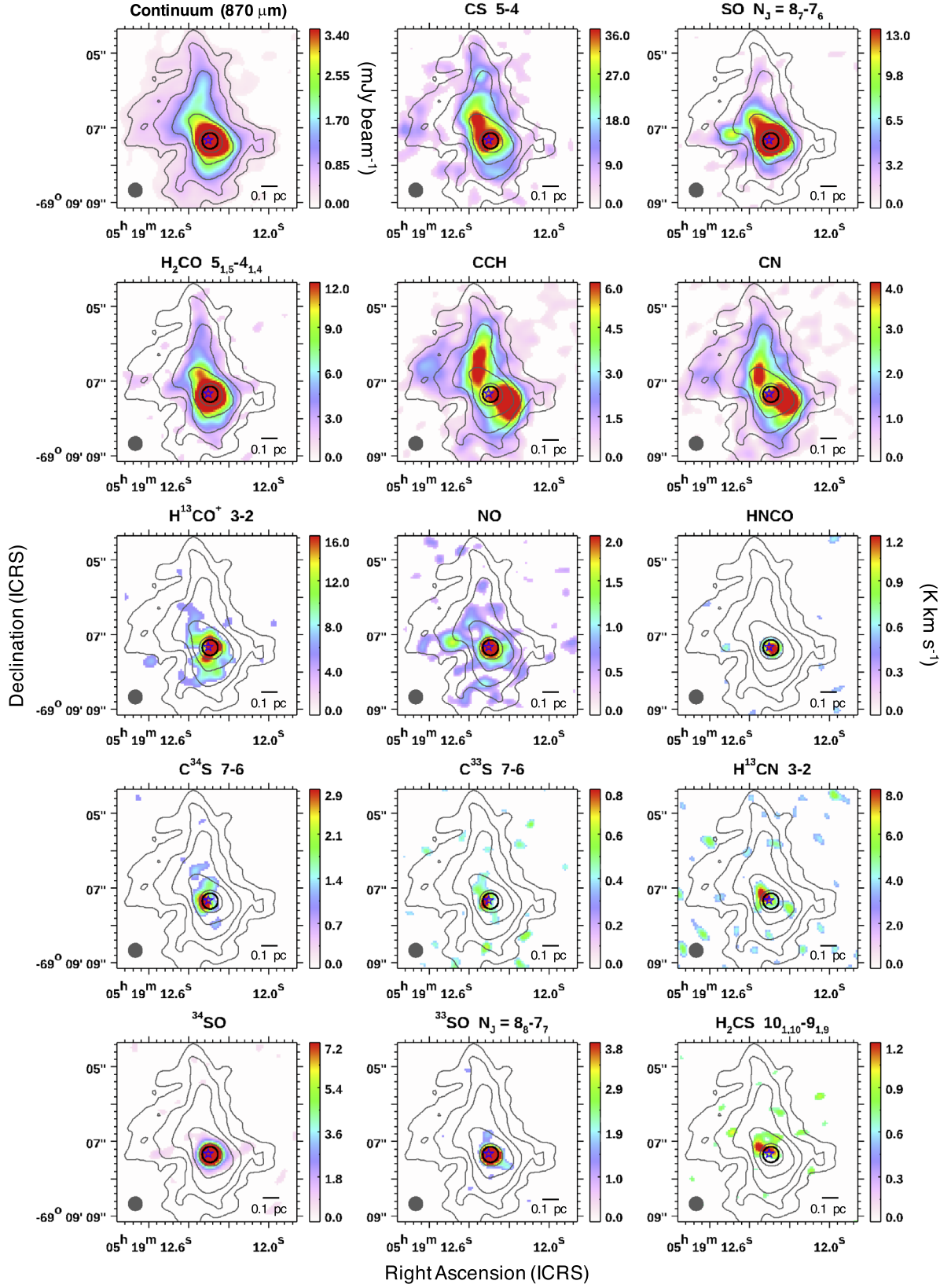


**Figure 3.** Flux distributions of the ALMA 870  $\mu\text{m}$  continuum and integrated intensity distributions of molecular emission lines. For CCH, CN, NO, HNCO, and  $^{34}\text{SO}$ , the detected multiple transitions are averaged. Gray contours represent the continuum distribution, and the contour levels are  $5\sigma$ ,  $10\sigma$ ,  $20\sigma$ ,  $40\sigma$ , and  $100\sigma$  of the rms noise ( $0.06 \text{ mJy/beam}$ ). Low signal-to-noise regions ( $S/N < 2$ ) are masked. The spectra discussed in the text are extracted from the region indicated by the thick black open circle. The blue open star represents the position of a high-mass YSO identified by infrared observations. The synthesized beam size is shown by the gray filled circle in each panel. North is up, and east is to the left.

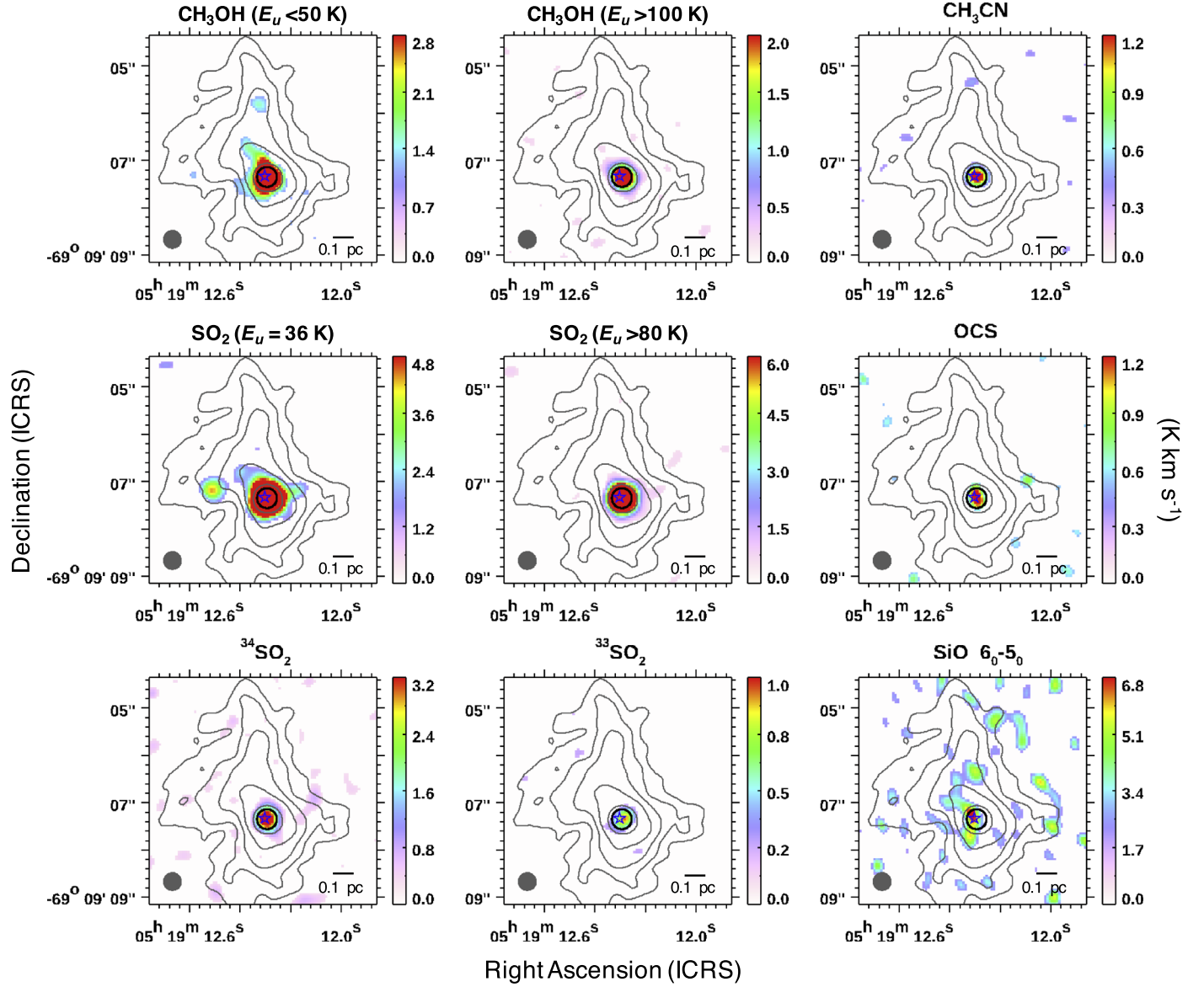


**Figure 4.** Same as in Figure 3. For CH<sub>3</sub>OH, CH<sub>3</sub>CN, SO<sub>2</sub>, OCS, <sup>34</sup>SO<sub>2</sub>, <sup>33</sup>SO<sub>2</sub>, the detected multiple transitions are averaged. CH<sub>3</sub>OH and SO<sub>2</sub> are separated into high- $E_u$  ( $>100$  K for CH<sub>3</sub>OH and  $>80$  K for SO<sub>2</sub>) and low- $E_u$  ( $<50$  K for CH<sub>3</sub>OH and  $=36$  K for SO<sub>2</sub>) components.

the transitions with  $E_u > 100$  K to fit the higher-temperature component, respectively. Derived column densities and rotation temperatures are summarized in Table 2. These rotation analyses suggest that the line of sight toward ST16 harbors two temperature components: (1) a hot-gas component with  $T_{\text{rot}} \sim 150$  K (an average temperature of high-temperature CH<sub>3</sub>OH, high-temperature SO<sub>2</sub>, <sup>34</sup>SO<sub>2</sub>, and <sup>33</sup>SO<sub>2</sub>) and (2) a warm gas component with  $T_{\text{rot}} \sim 50$  K (an average temperature of low-temperature CH<sub>3</sub>OH, low-temperature SO<sub>2</sub>, <sup>34</sup>SO, OCS, and CH<sub>3</sub>CN).

Note that the temperature and column density derived from the rotation diagram of SO would not be reliable, because the SO(6<sub>6</sub>–5<sub>5</sub>) and (8<sub>7</sub>–7<sub>6</sub>) lines are moderately optically thick ( $\tau \sim 0.3$ –1, with  $T_{\text{rot}} = 50$ –20 K and a beam filling factor of unity). Given a possible beam dilution effect for high excitation lines, their optical thickness would cause nonnegligible uncertainty on the reliability of the rotation analysis. We thus derive the SO column density using the SO(3<sub>3</sub>–2<sub>2</sub>) line, which has an  $S\mu^2$  value about 100 times smaller than the above two

transitions and is optically thin. Here, the rotation temperature is assumed to be the same as that of <sup>34</sup>SO ( $\sim 50$  K).

We have also estimated the rotational temperature of SO at the off-hot-core position (i.e., the  $0''.40$  diameter circular region centered at R.A. =  $05^{\text{h}}19^{\text{m}}12^{\text{s}}.39$  and decl. =  $-69^{\circ}9'6''.6$ ). Here, we derive  $T_{\text{rot}} = 24.5 \pm 1.4$  K and  $N = 4.2 \pm 0.6 \times 10^{14} \text{ cm}^{-2}$  (Figure 5, lower right panel). Note that the SO lines at the off position are optically thin ( $<0.15$ ), since the peak intensities are nearly five times lower than those at the hot core position. The derived  $T_{\text{rot}}$  would represent the temperature of the relatively cold and dense gas surrounding the hot core.

#### 4.2. Column Densities of Other Molecules

Column densities of molecular species other than those described in Section 4.1 are estimated from Equation (1) after solving it for  $N$ . For this purpose, we need to assume their rotation temperatures.

The rotation temperature of <sup>34</sup>SO ( $\sim 50$  K) corresponds to the temperature of warm components in the line of sight. This

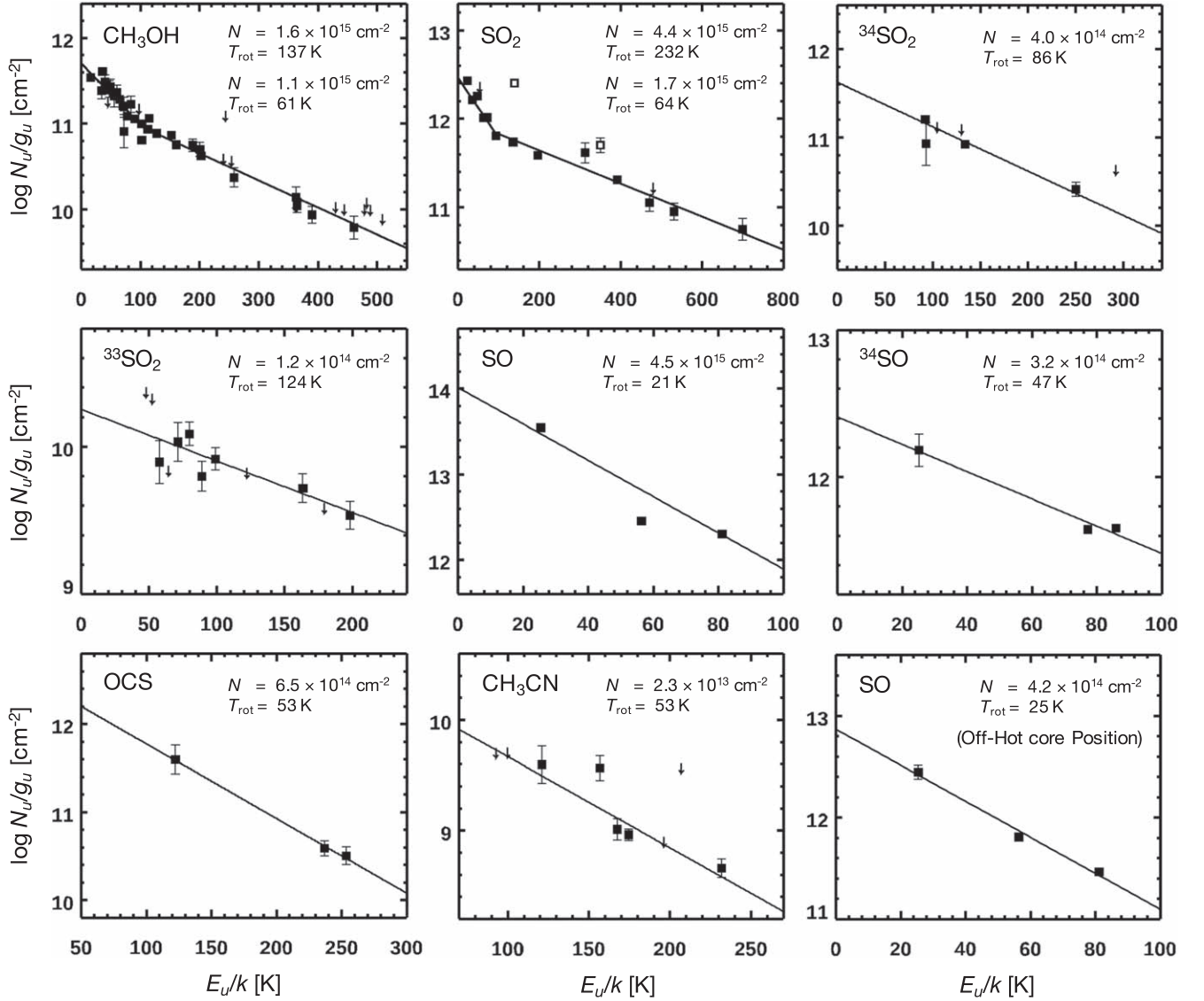


**Figure 5.** Rotation diagrams for  $\text{CH}_3\text{OH}$ ,  $\text{SO}_2$ ,  $^{34}\text{SO}_2$ ,  $^{33}\text{SO}_2$ ,  $\text{SO}$ ,  $^{34}\text{SO}$ ,  $\text{OCS}$ , and  $\text{CH}_3\text{CN}$  lines. Upper limit points are shown by the downward arrows. The solid lines represent the fitted straight line. Derived column densities and rotation temperatures are shown in each panel. For  $\text{CH}_3\text{OH}$  and  $\text{SO}_2$ , the left line is fitted using the transitions with  $E_u < 100$  K, while the right one is fitted using the transitions with  $E_u > 100$  K. Note that A- and E-state  $\text{CH}_3\text{OH}$  are fitted simultaneously. Two  $\text{SO}_2$  transitions,  $10_{6,4}-11_{5,7}$  and  $26_{3,23}-25_{4,22}$  (indicated by the open squares), are excluded from the fit, because they significantly deviate from other data points. At the lower right panel, the rotation diagram of  $\text{SO}$  at the off-hot core position is shown. See Section 4.1 for details.

temperature is applied to  $\text{SO}$  and  $^{33}\text{SO}$  considering the co-existence of isotopologues.  $\text{CS}$  shows an extended distribution similar to  $\text{SO}$ ; thus, we also applied  $T_{\text{rot}} = 50$  K for  $\text{CS}$ ,  $\text{C}^{34}\text{S}$ , and  $\text{C}^{33}\text{S}$ . Furthermore, we also assume  $T_{\text{rot}} = 50$  K for  $\text{CCH}$  and  $\text{CN}$ , because they are clearly extended and not centered at the hot core region. For other molecules that are concentrated at the hot core, we assume  $T_{\text{rot}} = 100$  K, which is an average temperature of the hot and warm gas components describe in Section 4.1.

We use the spectroscopic constants and partition functions extracted from the CDMS database except for  $\text{HCOOCH}_3$ , whose molecular data is extracted from the JPL database. Estimated column densities are summarized in Table 2.

We have also performed non-LTE calculation for column densities of selected species using RADEX (van der Tak et al. 2007). For input parameters, we use the  $\text{H}_2$  gas density of  $3 \times 10^6 \text{ cm}^{-3}$  according to our estimate in Section 4.3.4 and the background temperature of 2.73 K. Kinetic temperatures

are assumed to be the same as temperatures tabulated in Table 2. The line widths used in the analysis are taken from the tables in Appendix A. The resultant column densities are summarized in Table 2. The calculated non-LTE column densities are reasonably consistent with the LTE estimations.

#### 4.3. Column Density of $\text{H}_2$

A column density of molecular hydrogen ( $N_{\text{H}_2}$ ) is estimated by several methods to check its reliability. The  $\text{H}_2$  column densities derived by different methods are summarized in Table 3. Details of each method are described below.

##### 4.3.1. $N_{\text{H}_2}$ from the ALMA Continuum

The present ALMA dust continuum data can be used for the  $N_{\text{H}_2}$  estimate. The continuum brightness of ST16 is measured to be  $(3.37 \pm 0.34) \text{ mJy/beam}$  for  $1200 \mu\text{m}$  and  $(10.55 \pm 1.06) \text{ mJy/beam}$  for  $870 \mu\text{m}$  toward the region, the same as in the



**Table 2**  
Estimated Rotation Temperatures and Column Densities

Molecule	$T_{\text{rot}}$ (K)	$N(X)$ ( $\text{cm}^{-2}$ )	$N(X)$ non-LTE <sup>a</sup> ( $\text{cm}^{-2}$ )
$\text{CH}_3\text{OH}^b$ ( $E_u > 100$ K)	$137_{-7}^{+8}$	$(1.6_{-0.1}^{+0.1}) \times 10^{15}$	$(3.4 \pm 0.2) \times 10^{15}$
$\text{CH}_3\text{OH}^b$ ( $E_u < 100$ K)	$61_{-2}^{+2}$	$(1.1_{-0.1}^{+0.1}) \times 10^{15}$	$(1.6 \pm 0.1) \times 10^{15}$
$\text{SO}_2^b$ ( $E_u > 100$ K)	$232_{-22}^{+27}$	$(4.4_{-0.1}^{+0.1}) \times 10^{15}$	$(3.5 \pm 0.3) \times 10^{15}$
$\text{SO}_2^b$ ( $E_u < 100$ K)	$64_{-4}^{+5}$	$(1.7_{-0.1}^{+0.1}) \times 10^{15}$	$(2.0 \pm 0.1) \times 10^{15}$
$^{34}\text{SO}_2^b$	$86_{-9}^{+11}$	$(4.0_{-0.6}^{+0.8}) \times 10^{14}$	...
$^{33}\text{SO}_2^b$	$124_{-23}^{+37}$	$(1.2_{-0.2}^{+0.3}) \times 10^{14}$	...
$^{34}\text{SO}^{b,c}$	$47_{-14}^{+14}$	$(3.2_{-0.9}^{+0.9}) \times 10^{14}$	...
$\text{OCS}^b$	$53_{-8}^{+11}$	$(6.5_{-3.4}^{+7.2}) \times 10^{14}$	$(6.9 \pm 0.5) \times 10^{14}$
$\text{CH}_3\text{CN}^b$	$53_{-7}^{+10}$	$(2.3_{-1.0}^{+1.7}) \times 10^{13}$	$(2.5 \pm 0.2) \times 10^{13}$
$\text{SO}^d$	50	$(7.3 \pm 0.2) \times 10^{15}$	$(7.5 \pm 0.1) \times 10^{15}$
$^{33}\text{SO}$	50	$(1.4 \pm 0.1) \times 10^{14}$	...
$\text{CS}$	50	$(1.3 \pm 0.1) \times 10^{14}$	$(1.2 \pm 0.1) \times 10^{14}$
$\text{C}^{34}\text{S}$	50	$(6.7 \pm 0.4) \times 10^{12}$	...
$\text{C}^{33}\text{S}$	50	$(1.8 \pm 0.3) \times 10^{12}$	...
$\text{CCH}$	50	$(1.3 \pm 0.1) \times 10^{14}$	...
$\text{CN}$	50	$(4.5 \pm 0.5) \times 10^{13}$	...
$\text{H}_2\text{CO}$	100	$(2.1 \pm 0.1) \times 10^{14}$	$(1.3 \pm 0.1) \times 10^{14}$
$\text{H}^{13}\text{CO}^+$	100	$(1.4 \pm 0.1) \times 10^{13}$	$(7.7 \pm 0.3) \times 10^{12}$
$\text{NO}$	100	$(4.1 \pm 0.8) \times 10^{15}$	$(3.8 \pm 0.2) \times 10^{15}$
$\text{HNCO}$	100	$(3.7 \pm 0.8) \times 10^{13}$	$(2.3 \pm 0.2) \times 10^{13}$
$\text{H}^{13}\text{CN}$	100	$(8.8 \pm 2.0) \times 10^{12}$	$(4.2 \pm 0.2) \times 10^{12}$
$\text{HC}_3\text{N}$	100	$< 1.1 \times 10^{13}$	...
$\text{H}_2\text{CS}$	100	$(1.9 \pm 0.4) \times 10^{13}$	$(1.3 \pm 0.2) \times 10^{13}$
$\text{SiO}$	100	$(8.5 \pm 3.2) \times 10^{12}$	$(6.0 \pm 1.0) \times 10^{12}$
$\text{HDO}$	100	$< 3.8 \times 10^{14}$	...
$\text{c-C}_3\text{H}_2$	100	$< 2.4 \times 10^{14}$	...
$\text{C}_2\text{H}_5\text{OH}$	100	$< 4.1 \times 10^{14}$	...
$\text{C}_2\text{H}_5\text{CN}$	100	$< 4.5 \times 10^{14}$	...
$\text{CH}_3\text{OCH}_3$	100	$< 2.5 \times 10^{14}$	...
$\text{HCOOCH}_3$	100	$< 6.8 \times 10^{14}$	...
$\text{trans-HCOOH}$	100	$< 7.5 \times 10^{13}$	...

**Notes.** Uncertainties and upper limits are of the  $2\sigma$  level and do not include systematic errors due to adopted spectroscopic constants. See Sections 4.1 and 4.2 for details.

<sup>a</sup> The following lines are used for non-LTE calculation with RADEX;  $\text{CH}_3\text{OH}(7_2 \text{ A}^+_{-62} \text{ A}^+)$ ,  $\text{CH}_3\text{OH}(5_1 \text{ E}-4_1 \text{ E})$ ,  $\text{SO}_2(5_{3,3}-4_{2,2})$ ,  $\text{SO}_2(14_{0,14}-13_{1,13})$ ,  $\text{OCS}(28-27)$ ,  $\text{CH}_3\text{CN}(19_{0-18_0})$ ,  $\text{SO}(N_f = 6_6-5_5)$ ,  $\text{CS}(5-4)$ ,  $\text{H}_2\text{CO}(5_{1,5}-4_{1,4})$ ,  $\text{H}^{13}\text{CO}^+(3-2)$ ,  $\text{NO}(J = \frac{7}{2}-\frac{5}{2})$ ,  $\Omega = \frac{1}{2}$ ,  $F = \frac{9}{2} + \frac{7}{2}$ ),  $\text{HNCO}(16_{0,16}-15_{0,15})$ ,  $\text{H}^{13}\text{CN}(3-2)$ ,  $\text{H}_2\text{CS}(10_{1,10}-9_{1,9})$ , and  $\text{SiO}(6-5)$ .

<sup>b</sup> Derived based on the rotation diagram analysis.

<sup>c</sup> Assumed empirical 30% uncertainty for  $T_{\text{rot}}$  and  $N$  because of the fitted data points are relatively few and scattered.

<sup>d</sup> Derived from the  $\text{SO}(3_3-2_3)$  line.

spectral extraction<sup>13</sup>. Based on the standard treatment of optically thin dust emission, we use the following equation to calculate  $N_{\text{H}_2}$ :

$$N_{\text{H}_2} = \frac{F_\nu / \Omega}{2\kappa_\nu B_\nu(T_d) Z \mu m_{\text{H}}}, \quad (3)$$

where  $F_\nu / \Omega$  is the continuum flux density per beam solid angle as estimated from the observations,  $\kappa_\nu$  is the mass absorption coefficient of dust grains coated by thin ice

mantles at  $1200/870 \mu\text{m}$  as taken from Ossenkopf & Henning (1994). We here use  $1.06 \text{ cm}^2 \text{ g}^{-1}$  for  $1200 \mu\text{m}$  and  $1.89 \text{ cm}^2 \text{ g}^{-1}$  for  $870 \mu\text{m}$ ,  $T_d$  is the dust temperature, and  $B_\nu(T_d)$  is the Planck function,  $Z$  is the dust-to-gas mass ratio,  $\mu$  is the mean atomic mass per hydrogen (1.41, according to Cox 2000), and  $m_{\text{H}}$  is the hydrogen mass. We use the dust-to-gas mass ratio of 0.0027 for the LMC, which is obtained by scaling the Galactic value of 0.008 by the metallicity of the LMC ( $\sim 1/3 Z_\odot$ ).

The dust temperature is a key assumption for the derivation of  $N_{\text{H}_2}$ . We estimate  $N_{\text{H}_2}$  for three different dust temperatures, 20, 60, and 150 K, as shown in Table 3. We revisit the validity of these assumption in Section 4.3.4, based on the comparison of  $N_{\text{H}_2}$  values by different methods. Note that consistent  $N_{\text{H}_2}$  values are derived from the 870 and  $1200 \mu\text{m}$  continuum, suggesting that the submillimeter continuum emission from ST16 is almost dominated by the thermal emission from dust grains.

#### 4.3.2. $N_{\text{H}_2}$ from the SED Fit

A model fit to the source's SED provides us with an alternative way to estimate the total gas column density in the line of sight. We have tested two SED models in this work: one by Robitaille et al. (2007) and another by Zhang & Tan (2018). For input data, we use 1–1200  $\mu\text{m}$  photometric and spectroscopic data of ST16 as shown in Figure 1. We exclude the SPIRE 350 and  $500 \mu\text{m}$  band data in the fit, because they are possibly contaminated by diffuse emission around the YSO due to their large point-spread function (about  $27''$  and  $41''$  in FWHM, respectively). The distance to ST16 is assumed to be the same as that of the LMC.

The model of Robitaille et al. (2007) produces a bunch of fitted SEDs that differ in  $\chi^2$  values. To obtain a range of acceptable fits, we use a cutoff value for  $\chi^2$  that is described in Robitaille et al. (2007). We select the fit results, which have  $(\chi^2 - \chi^2_{\text{best}}) / N_{\text{data}} \leq 3$ , where  $\chi^2_{\text{best}}$  is the  $\chi^2$  value of the best-fit model and  $N_{\text{data}}$  is the total number of data points used for the fit. Then, a median value of the selected results is adopted as a representative value and their standard deviation is adopted as uncertainty.

In the Zhang & Tan (2018) model, the evolution of the protostar and its surroundings is structured in a self-consistent way based on the turbulent core accretion theory for massive star formation (McKee & Tan 2003). The best models are selected based on  $\chi^2$  values of the SED fits, as in the Robitaille model. We use the best five models to estimate the final column density and uncertainty, i.e., their average value and standard deviation.

In both models, the total visual extinction ( $A_V$ ) from the protostar to the observer is derived from the best-fit SEDs. The value is doubled in order to compare with submillimeter data, which probe the total column density in the line of sight. To estimate  $N_{\text{H}_2}$  values from the derived  $A_V$ , we use an  $N_{\text{H}_2}/A_V$  conversion factor. Koornneef (1982) reported  $N_{\text{H}}/E(B - V) = 2.0 \times 10^{22} \text{ cm}^{-2} \text{ mag}^{-1}$  and Fitzpatrick (1985) reported  $N_{\text{H}}/E(B - V) = 2.4 \times 10^{22} \text{ cm}^{-2} \text{ mag}^{-1}$  for the interstellar extinction in the LMC. Taking their average and adopting a slightly high  $A_V/E(B - V)$  ratio of  $\sim 4$  for dense clouds (Whittet et al. 2001), we obtain  $N_{\text{H}_2}/A_V = 2.8 \times 10^{21} \text{ cm}^{-2} \text{ mag}^{-1}$ , where we assume that all of the hydrogen atoms are in the form of  $\text{H}_2$ . The estimated  $N_{\text{H}_2}$  and  $A_V$  are summarized in Table 3. For both SED models, consistent  $N_{\text{H}_2}$  values are obtained.

<sup>13</sup> A canonical uncertainty of 10% for the absolute flux calibration of the ALMA Band 6 and 7 data is adopted (see ALMA Technical Handbook).



**Table 3**  
Estimated  $H_2$  Column Densities and  $A_V$

	ALMA Continuum						SED Fit		$\tau_{9.7}$
	$T_d = 20$ K		$T_d = 60$ K		$T_d = 150$ K		RW07 <sup>a</sup>	ZT18 <sup>b</sup>	
	870 $\mu\text{m}$	1200 $\mu\text{m}$	870 $\mu\text{m}$	1200 $\mu\text{m}$	870 $\mu\text{m}$	1200 $\mu\text{m}$			
$N_{\text{H}_2}$ ( $10^{23} \text{ cm}^{-2}$ )	$21.0 \pm 2.1$	$22.2 \pm 2.2$	$5.64 \pm 0.56$	$5.47 \pm 0.55$	$2.12 \pm 0.21$	$2.01 \pm 0.20$	$5.40 \pm 1.12$	$5.71 \pm 0.87$	$5.60 \pm 0.56$
$A_V$ (mag)	$749 \pm 75$	$792 \pm 79$	$202 \pm 20$	$195 \pm 20$	$76 \pm 8$	$72 \pm 7$	$193 \pm 40$	$204 \pm 31$	$200 \pm 20$

**Notes.** In this work, we use  $N_{H_2} = (5.6 \pm 0.6) \times 10^{23} \text{ cm}^{-2}$  as a representative value, which is the average of  $N_{H_2}$  derived by ALMA dust continuum (870 and 1200  $\mu\text{m}$  with  $T_d = 60$  K), the SED model fits, and the 9.7  $\mu\text{m}$  silicate dust absorption depth (see Section 4.3 for details). Uncertainties do not include systematic errors due to adopted optical constants.

<sup>a</sup> Robitaille et al. (2007).

<sup>b</sup> Zhang & Tan (2018).

#### 4.3.3. $N_{H_2}$ from the 9.7 $\mu\text{m}$ Silicate Dust Absorption

The mid-infrared spectrum of ST16 shows a deep absorption due to the silicate dust at 9.7  $\mu\text{m}$  (Figure 1). The peak optical depth of the 9.7  $\mu\text{m}$  silicate dust absorption band ( $\tau_{9.7}$ ) is estimated to be 2.44 from the spectrum. The relationship between the visual extinction ( $A_V$ ) and  $\tau_{9.7}$  reported for Galactic dense cores is

$$A_V = \frac{\tau_{9.7} - (0.12 \pm 0.05)}{0.21 \pm 0.02} \times 8.8 \quad (4)$$

according to Boogert et al. (2011; assuming  $A_V/A_K = 8.8$ ). Applying this relationship to ST16, we obtain  $A_V = 100 \pm 10$  mag. Because the present infrared absorption spectroscopy probes only the foreground component relative to the central protostar, the above  $A_V$  value should be doubled to compare with submillimeter data, which probe the total column density in the line of sight. Therefore, the total visual extinction expected from the 9.7  $\mu\text{m}$  silicate band is  $A_V = 200 \pm 20$  mag for ST16. Using the LMC's  $N_{H_2}/A_V$  ratio of  $2.8 \times 10^{21} \text{ cm}^{-2} \text{ mag}^{-1}$  described in Section 4.3.2, we obtain  $N_{H_2} = (5.60 \pm 0.56) \times 10^{23} \text{ cm}^{-2}$ .

#### 4.3.4. Recommended $H_2$ Column Density, Dust Extinction, and Gas Mass

The discussion in Sections 4.3.1–4.3.3 suggests that consistent  $N_{H_2}$  values are obtained by different methods; i.e., the SED fits by the Robitaille et al. (2007) and Zhang & Tan (2018) models, and the  $\tau_{9.7}$ – $A_V$  relation. In addition, the  $N_{H_2}$  estimates by the dust continuum with  $T_d = 60$  K result in consistent  $N_{H_2}$  values with the above methods. In this paper, we use  $N_{H_2} = (5.6 \pm 0.6) \times 10^{23} \text{ cm}^{-2}$  as a representative value, which corresponds to the average of  $N_{H_2}$  derived by dust continuum (870 and 1200  $\mu\text{m}$  with  $T_d = 60$  K), the SED model fits, and the 9.7  $\mu\text{m}$  silicate dust absorption depth. This  $N_{H_2}$  corresponds to  $A_V = 200$  mag using the  $N_{H_2}/A_V$  factor described in Section 4.3.2. Assuming the source diameter of 0.1 pc and the uniform spherical distribution of gas around a protostar, we estimate the average gas number density to be  $n_{H_2} = 3 \times 10^6 \text{ cm}^{-3}$  and the total gas mass to be  $100 M_\odot$ .

Here, we emphasize that the derived  $H_2$  value corresponds to the total column density integrated over the whole line of sight, which includes various temperature components. Thus, the assumed dust temperature ( $T_d = 60$  K) corresponds to the mass-weighted average temperature in the line of sight. Given the lower dust temperature compared with the gas temperature in the hot core region, the contribution from low-temperature component would not be negligible. The situation is the same

for Galactic hot core sources compared in this work, whose  $N_{H_2}$  values are derived by using low- $J$  CO isotopologue lines, and thus, the low-temperature component would have a nonnegligible contribution. To selectively probe the total gas column density in the high-temperature hot core region, observations of high- $J$  CO lines or  $H_2O$  lines will be important, which will be accessible by future far-infrared facilities.

#### 4.4. Fractional Abundances

Fractional abundances of molecules relative to  $H_2$  are summarized in Table 4, which are calculated by using the molecular column densities estimated in Section 4.2 and  $N_{H_2}$  estimated in Section 4.3. Abundances of HCN and  $HCO^+$  are estimated from their isotopologues  $H^{13}CN$  and  $H^{13}CO^+$ , assuming  $^{12}C/^{13}C = 49$  (Wang et al. 2009).

### 5. Discussion

#### 5.1. Hot Molecular Core Associated with ST16

A variety of molecular emission lines, including high-excitation lines of typical hot core tracers such as  $CH_3OH$  and  $SO_2$ , are detected from the line of sight toward a high-mass YSO, ST16 ( $L = 3 \times 10^5 L_\odot$ , Figure 1). The source is associated with high-density gas, as the  $H_2$  gas density is estimated to be  $n_{H_2} = 3 \times 10^6 \text{ cm}^{-3}$  based on the dust continuum data (Section 4.3.4). According to the rotation analyses of  $CH_3OH$  and  $SO_2$  (Figure 5), the temperature of molecular gas is estimated to be higher than 100 K, which is sufficient to trigger the sublimation of ice mantles. The size of the hot-gas-emitting region is as compact as  $\sim 0.1$  pc, according to integrated intensity maps shown in Figures 3 and 4. Note that the line of sight toward ST16 also contains compact and warm ( $\sim 50$ – $60$  K) gas components as seen in the rotation diagrams of  $CH_3OH$ ,  $SO_2$ ,  $^{34}SO$ ,  $OCS$ , and  $CH_3CN$ . In addition, the source is surrounded by relatively extended and cold ( $\sim 25$  K) gas components, as represented by the rotation diagram of  $SO$  at the off-center position. The nature of ST16, (i) the compact source size, (ii) the high gas temperature, (iii) the high density, (iv) the association with a high-mass YSO, and (v) the presence of chemically rich molecular gas strongly suggest that the source is associated with a hot molecular core. The temperature structure and the molecular distribution in ST16 are illustrated in Figure 6 based on the present observational results.

#### 5.2. Molecular Abundances

Figure 7 shows a comparison of molecular abundances between the ST16 hot core and Galactic hot cores (Orion and W3 ( $H_2O$ )).



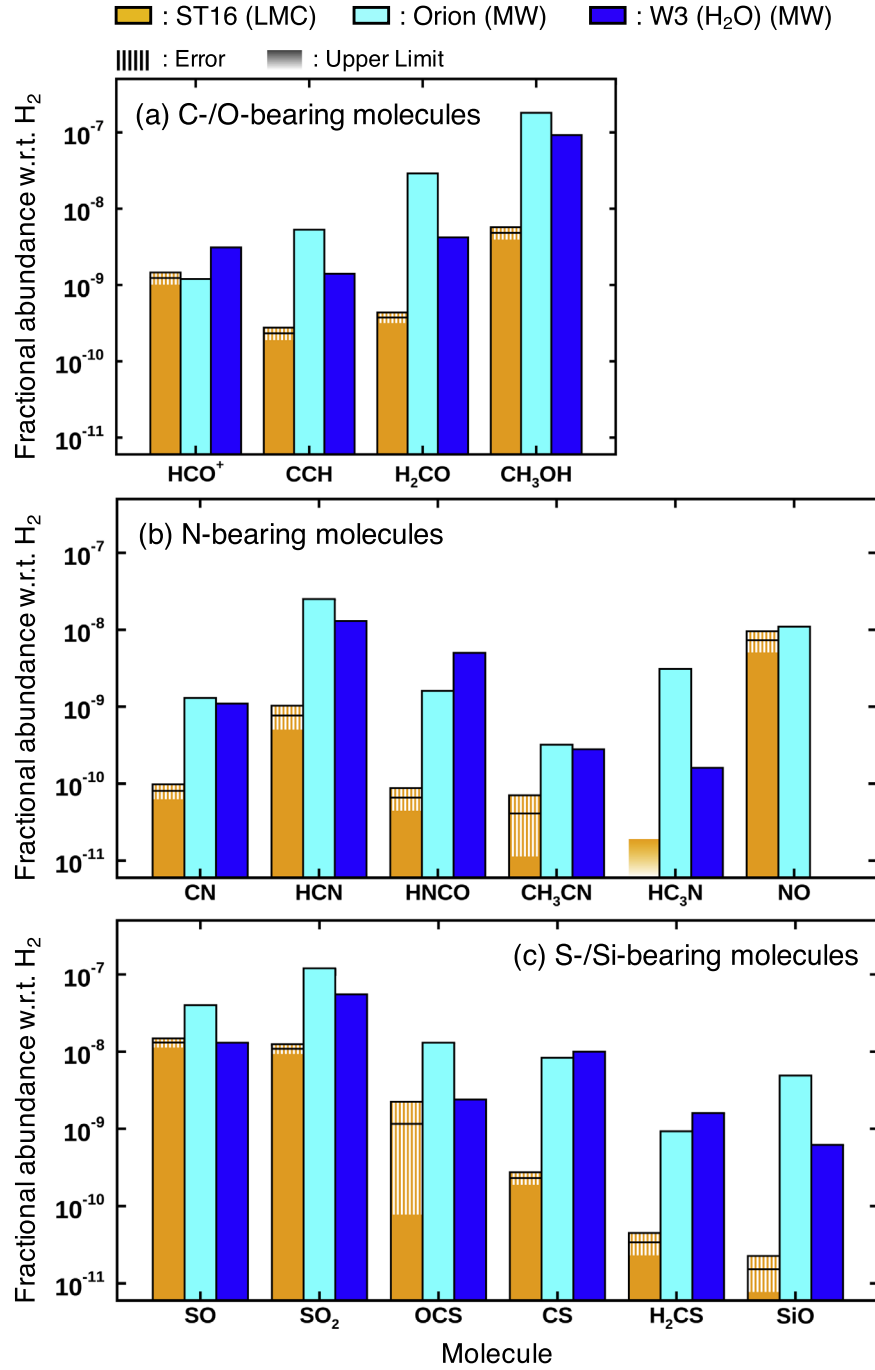


**Figure 7.** Comparison of molecular abundances between an LMC hot core (ST16: orange) and Galactic hot cores (Orion: cyan and W3 ( $\text{H}_2\text{O}$ ): blue). Each panel shows (a) carbon- and oxygen-bearing molecules ( $\text{HCO}^+$ , CCH,  $\text{H}_2\text{CO}$ , and  $\text{CH}_3\text{OH}$ ); (b) nitrogen-bearing molecules (CN, HCN, HNCO,  $\text{CH}_3\text{CN}$ ,  $\text{HC}_3\text{N}$ , and NO); (c) sulfur- and silicon-bearing molecules (SO,  $\text{SO}_2$ , OCS, CS,  $\text{H}_2\text{CS}$ , and SiO). The area with thin vertical lines indicate the error bar. The bars with a color gradient indicate an upper limit. The plotted data are summarized in Table 4 for ST16, while those for Galactic hot cores are collected from the literature (see Section 5.2).

LMC inhibit the hydrogenation of CO in ice-forming dense clouds, which leads to the low abundances of organic molecules that are mainly formed on grain surfaces ( $\text{CH}_3\text{OH}$ , HNCO, and partially  $\text{H}_2\text{CO}$ ). Therefore, the different chemical history during the ice formation stage could contribute to the differentiation of organic-poor and organic-rich hot cores in low-metallicity environments. Alternatively, the difference in the hot core's evolutionary stage may contribute to the observed chemical diversity, since high-temperature gas-phase chemistry can also decrease the  $\text{CH}_3\text{OH}$  abundance at a late stage (e.g., Nomura & Millar 2004; Garrod & Herbst 2006; Vasyunin & Herbst 2013; Balucani et al. 2015).

The compact spatial distribution of  $\text{CH}_3\text{OH}$  lines in ST16 suggests its grain surface origin, as the emission is concentrated at the hot core position (Figure 4). On the other hand, the  $\text{H}_2\text{CO}$  emission is relatively extended around the hot core. This would suggest that  $\text{H}_2\text{CO}$  can also be formed efficiently in the gas phase, as in Galactic star-forming regions (e.g., van der Tak et al. 2000).

$\text{SO}_2$  is suggested to be a useful molecular tracer for the study of hot core chemistry at low metallicity, according to the ALMA observations of the ST11 hot core (Shimonishi et al. 2016b). This is because (i)  $\text{SO}_2$  mainly originates from the hot core region as suggested from its compact distribution and high rotation



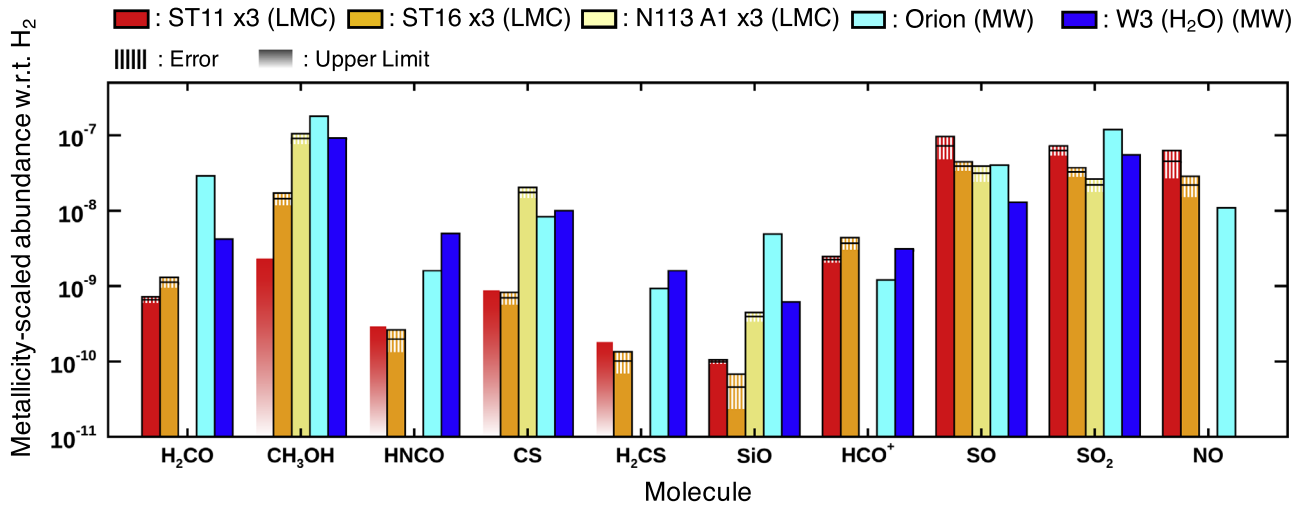


**Figure 8.** Comparison of metallicity-scaled molecular abundances between three LMC hot cores (ST11: red, ST16: orange, and N113 A1: light yellow) and Galactic hot cores (Orion: cyan and W3 (H<sub>2</sub>O): blue). Abundances of LMC hot cores are multiplied by three to correct for the metallicity difference relative to Galactic ones. The area with thin vertical lines indicate the error bar. The bar with a color gradient indicate an upper limit. The data for N113 A1 are adapted from Sewilo et al. (2018). See Section 5.2 for details.

temperature, (ii) the abundance of SO<sub>2</sub> simply scales with metallicity (the metallicity-scaling law), and (iii) SO<sub>2</sub> and its isotopologues show a large number of emission lines even in a limited frequency coverage. The same characteristics are observed in the present ST16 hot core. Metallicity-scaled abundances of SO<sub>2</sub> in LMC hot cores (ST11, ST16, N113 A1) are similar to each other and almost comparable with those of Galactic hot cores (Figure 8). This is remarkably in contrast to the abundance of a classical hot core tracer, CH<sub>3</sub>OH, which shows a large variation in the low-metallicity environment of the LMC. The above characteristic behavior of SO<sub>2</sub> suggests that high-excitation SO<sub>2</sub> lines will be a useful tracer of metal-poor hot core chemistry.

The metallicity-scaling law of SO<sub>2</sub> is not applicable to other sulfur-bearing molecules, as CS and H<sub>2</sub>CS are significantly less abundant in organic-poor LMC hot cores. The metallicity-scaled abundances of SO in LMC hot cores are comparable with Galactic values, as in SO<sub>2</sub>. However, the low rotation temperature and the extended spatial distribution of SO would suggest that it is widely distributed beyond the hot core region.

NO may be an interesting molecule that is efficiently produced in low-metallicity environments. An overabundance of NO is reported for the ST11 hot core in the LMC (Shimonishi et al. 2016b). Interestingly, a similar trend is observed in the present hot core. The metallicity-scaled abundance histogram shows that the NO abundances in LMC hot cores are higher than that in Orion, despite the low abundance of elemental nitrogen in the LMC (Figure 8). Note the plotted NO abundance of Orion is  $1.1 \times 10^{-8}$ , while the average and the standard deviation of NO abundances in six Galactic high-mass star-forming region is  $(8.2 \pm 0.3) \times 10^{-9}$  (Ziurys et al. 1991). Currently, such a high abundance of nitrogen-bearing species is seen only in NO, as all of the other nitrogen-bearing molecules detected in ST16 are less abundant than those of Galactic hot cores (Figure 7(b)).

The expected strength ratio of NO lines at 351.04352 and 351.05171 GHz in the LTE and optically thin case is 1.00 : 1.27, while the observed integrated intensity ratio is  $(1.00 \pm 0.19) : (1.35 \pm 0.10)$  based on the data in Table 7. Thus, the observed NO lines are presumably optically thin.

The distribution of NO is mainly concentrated at the hot core position, but slightly extended components are also seen at the east

side of the hot core. The abundance of NO at the hot core position is  $(7.3 \pm 2.2) \times 10^{-9}$  (see Table 4). At the secondary peak on the east side, the abundance is estimated to be  $(7.5 \pm 2.2) \times 10^{-9}$ , where we assume  $T_{\text{rot}} = T_d = 22$  K based on the rotation analysis of SO, and with this temperature, we have derived  $N(\text{NO}) = (1.2 \pm 0.2) \times 10^{15} \text{ cm}^{-2}$  and  $N_{\text{H}_2} = (1.6 \pm 0.2) \times 10^{23} \text{ cm}^{-2}$ . Similar abundances of NO between the hot core and the nearby peak may suggest a common chemical origin.

### 5.3. Astrochemical Simulations

In this section, we use astrochemical simulations to interpret the observed chemical characteristics of low-metallicity hot cores in the LMC. The simulations include a gas-grain chemical network coupled with a toy physical model, aiming at simulating the chemical evolution of a star-forming core up to the hot core stage. We here consider three different evolutionary stages (i.e., cold, warm-up, and post-warm-up), where physical conditions (density, temperature, and extinction) vary at each stage. The first stage corresponds to the quiescent cold cloud, the second stage mimics the collapsing and warming-up core, and the third stage corresponds to the high-temperature core before the formation of H II region. The second and third stages correspond to the hot core. Two different setups for initial elemental abundances and gas-to-dust ratio are considered to simulate hot core chemistry at the LMC and Galactic conditions. Details of our astrochemical simulations are described in Appendix C.

The chemical history during the ice-forming stage is suggested to play an important role in subsequent hot core chemistry (Section 5.2). Thus, here we focus on the effect of initial physical conditions on the chemical compositions of a hot core. In the astrochemical simulations, we have varied the dust extinction parameter ( $A_V$ ) at the first cold stage and examined how the subsequent hot core compositions are affected. Here,  $A_V$  values are coupled with grain temperature using Equation (5) in Appendix C.

Figure 9 shows the peak molecular abundances that are achieved during the hot core stage. The plotted peak abundances corresponds to the maximum achievable abundances of hot cores at each condition since hot core chemistry is time-dependent.

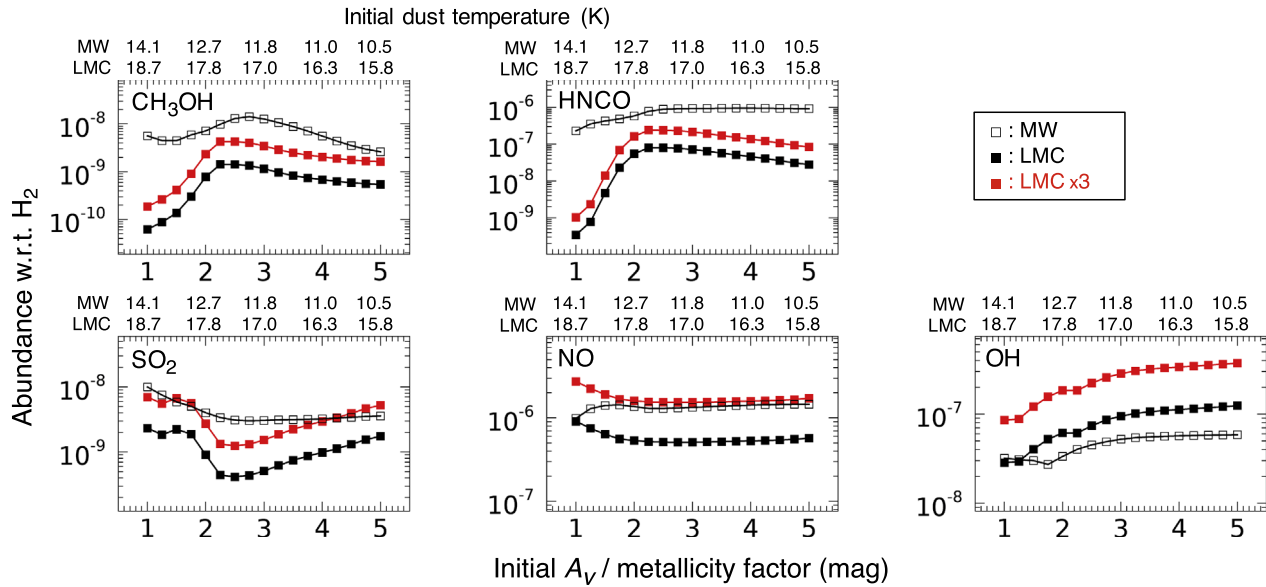


**Figure 9.** Simulated peak molecular abundances of  $\text{CH}_3\text{OH}$ ,  $\text{HNCO}$ ,  $\text{SO}_2$ ,  $\text{NO}$ , and  $\text{OH}$  during the hot core stage plotted against the initial dust extinction at the prestellar stage. The corresponding dust temperature is also plotted at the upper axis in each panel. Note that, for LMC simulations,  $A_V$  values are divided by three (metallicity factor) to mimic the low dust-to-gas ratio.  $A_V/(\text{metallicity factor}) = 1$  mag corresponds to the gas column density of  $N_{\text{H}_2} = 2.8 \times 10^{21} \text{ cm}^{-2}$  using the  $N_{\text{H}_2}/A_V$  conversion factor in Section 4.3.2. Results of hot core simulations for the Galactic case (open squares) and the LMC case (filled square) are plotted. The red filled squares represent the metallicity-scaled abundances for the LMC case, where the abundances are multiplied by three.

It is seen from the figure that the maximum achievable abundances of  $\text{CH}_3\text{OH}$  gas in a hot core significantly decrease as the visual extinction of the first cold stage (ice-forming stage) decreases. The decrease of the abundance at the low  $A_V$  regime is particularly enhanced in the LMC condition.

The main reason behind this is because the abundance of solid  $\text{CH}_3\text{OH}$  is sensitive to the dust temperature. As discussed in the previous section,  $\text{CH}_3\text{OH}$  is mainly formed by the grain surface reaction at the cold stage, and then released into the gas-phase at the hot core stage. The hydrogenation reaction of CO mainly controls the formation of  $\text{CH}_3\text{OH}$  on surfaces, but this reaction is inhibited when the grain surface temperature increases, because of the high volatility of atomic hydrogen. The effect is enhanced in the LMC case, because of the lower  $A_V$  at the ice-forming stage, which leads to the higher dust temperature. A similar behavior is also seen in  $\text{HNCO}$ , suggesting the importance of hydrogenation for its production. The present simulations are consistent with the picture provided by the warm ice chemistry hypothesis (Shimonishi et al. 2016a, 2016b) and previous astrochemical simulations dedicated to the LMC condition (Acharyya & Herbst 2015, 2018; Pauly & Garrod 2018).

At the high  $A_V$  regime, the peak  $\text{CH}_3\text{OH}$  abundances of the LMC case gradually approaches to the metallicity-corrected Galactic  $\text{CH}_3\text{OH}$  abundances. This could be because, in both LMC and Galactic cases, the grain surface is cold enough to trigger the CO hydrogenation, and the resultant  $\text{CH}_3\text{OH}$  abundances are regulated by the elemental abundances.

The present astrochemical simulations suggest that a large chemical diversity of organic molecules seen in LMC hot cores is related to the different physical condition at the initial stage of star formation. Particular organic molecules such as  $\text{CH}_3\text{OH}$  and  $\text{HNCO}$  decrease when a prestellar ice-forming cloud is less shielded, because of the inhibited surface hydrogenation reaction at increased dust temperature. This effect is particularly enhanced in a low-metallicity condition due to the low dust content in a star-forming core.

Molecular species that are mainly produced by high-temperature gas-phase chemistry show different behavior.  $\text{SO}_2$  is one of those cases. It is suggested to be a key hot core tracer at low metallicity since the metallicity-scaling law can apply to its abundances (see Section 5.2). Such a tendency is seen in the present simulation results. The peak abundances of  $\text{SO}_2$  in a hot core, after corrected for the metallicity, are nearly comparable with Galactic cases (Figure 9). Also,  $\text{SO}_2$  abundances are less affected by the initial  $A_V$  at the ice-forming stage.

A major molecular reservoir of sulfur in the cold stage is solid  $\text{H}_2\text{S}$  in our simulations. It is released into the gas phase at the hot core stage and experiences subsequent chemical syntheses into  $\text{SO}_2$ ; i.e.,  $\text{H}_2\text{S} \xrightarrow{\text{H}} \text{SH} \xrightarrow{\text{H}} \text{S} \xrightarrow{\text{OH/O}_2} \text{SO} \xrightarrow{\text{OH}} \text{SO}_2$  (e.g., Charnley 1997; Nomura & Millar 2004). This chemical sequence can reset the ice compositions that were accumulated at the cold stage and help initialize a major sulfur reservoir into atomic sulfur. Atomic sulfur is further synthesized into  $\text{SO}_2$ , but since it is a major product, the  $\text{SO}_2$  abundance might be directly regulated by the elemental abundance of sulfur, which is roughly proportional to the metallicity. We speculate this *reset* effect contributes to metallicity-scaled hot core compositions of particular molecular species.

$\text{NO}$  in hot cores is also suggested to be mainly formed by high-temperature gas-phase chemistry, which is the neutral-neutral reaction between N and OH (e.g., Herbst & Klemperer 1973; Pineau des Forets et al. 1990; Nomura & Millar 2004). A major molecular reservoir of nitrogen in the cold stage is either solid  $\text{N}_2$  or  $\text{NH}_3$  in our simulations. Likewise  $\text{SO}_2$ , the parent species leading to the formation of  $\text{NO}$  would experience the chemical reset at the hot core stage. This could be the reason why  $\text{NO}$  abundances in a hot core are less affected by the physical condition of the initial ice-forming stage (Figure 9).

Note that the simulated peak  $\text{NO}$  abundances in the LMC case become comparable with those of the Galactic case at the low  $A_V$  regime. The behavior is consistent with the present observations, as LMC hot cores show  $\text{NO}$  abundances that are nearly comparable with Galactic hot cores despite the low nitrogen

**Table 5**  
Ice Abundances Toward ST16

	H <sub>2</sub> O Ice	CO <sub>2</sub> Ice	CO Ice	CH <sub>3</sub> OH Ice
$N(X)$ ( $10^{17}$ cm <sup>-2</sup> )	$19.6 \pm 3.2$	$2.7 \pm 0.2$	$<2$	$<1.2$
$N(X)/N_{\text{H}_2}$	$(3.5 \pm 1.0) \times 10^{-6}$	$(4.8 \pm 1.7) \times 10^{-7}$	$<4 \times 10^{-7}$	$<2.4 \times 10^{-7}$

**Note.** Tabulated ice abundances are adapted from Shimonishi et al. (2016a). We use  $N_{\text{H}_2} = (5.6 \pm 0.6) \times 10^{23}$  cm<sup>-2</sup> based on this work.

abundance. We speculate that the increased production of gaseous OH at the hot core stage may contribute to this, since peak OH abundances are higher in the LMC simulations, as shown in Figure 9. The efficient production of OH could be related to lower O/H or O/H<sub>2</sub> ratios at low metallicity. Alternatively, the increased production of solid NO at the prestellar stage may also contribute to the overproduction of NO in LMC hot cores. Gas-grain astrochemical simulations of a cold molecular cloud with a new set of atomic binding energies actually have reported the increase of solid NO according to the increased grain temperature (Shimonishi et al. 2018a).

More detailed and sophisticated astrochemical simulations of low-metallicity hot cores, involving the latest chemical data and various physicochemical mechanisms, are required for more quantitative interpretation of observed hot core compositions at different metallicity. Further simulations will be presented in a future paper.

#### 5.4. Infrared Spectral Characteristics of ST16

The observed hot core region corresponds to the infrared center of ST16. No emission line components (i.e., hydrogen recombination lines or fine-structure lines from ionized metals) are seen in the near- to mid-infrared spectrum of ST16 (Seale et al. 2009; Shimonishi et al. 2016a). Despite the high bolometric luminosity, the source is still in an early evolutionary stage before the formation of a prominent H II region. This would indicate that the central massive protostar has a low effective temperature ( $<10,000$  K) and large radius ( $>100 R_{\odot}$ ), which is theoretically predicted in the case of a high accretion rate with  $>10^{-3} M_{\odot} \text{ yr}^{-1}$  (Hosokawa & Omukai 2009; Tanaka et al. 2018).

Abundances of solid molecules in the line of sight toward the infrared center of ST16 are summarized in Table 5. Elemental abundances of gas-phase oxygen and carbon in dense clouds in the LMC, after considering the depletion into dust grain material, are estimated to be  $4.0 \times 10^{-5}$  for oxygen and  $1.5 \times 10^{-5}$  for carbon (w.r.t. H<sub>2</sub>), according to the LMC's low-metal abundance model presented in Acharyya & Herbst (2015). The total fractional abundance of elemental oxygen in solid H<sub>2</sub>O and CO<sub>2</sub> (w.r.t. H<sub>2</sub>) in ST16 is about  $4.5 \times 10^{-6}$ . This would suggest that a nonnegligible fraction ( $\sim 10\%$ ) of elemental oxygen still remains in ices in the direction of ST16. Because the temperature of the hot core region is high enough for the ice sublimation, these ices would exist in ST16's cold outer envelope that is located at the foreground side to the observer. Note that, for more comprehensive estimates of the gas/ice ratio, future observations of gas-phase H<sub>2</sub>O, CO<sub>2</sub>, and CO will be important.

#### 5.5. Isotope Abundances of Sulfur

Isotope abundances of <sup>32</sup>S, <sup>34</sup>S, and <sup>33</sup>S, based on the present observations of SO, SO<sub>2</sub>, CS, and their isotopologues, are summarized in Table 6.

The <sup>32</sup>S/<sup>34</sup>S ratios for SO and SO<sub>2</sub> (23 and 15) in ST16 are well consistent with those estimated for the ST11 hot core and the

N113 star-forming region in previous studies ( $\sim 15$ , Wang et al. 2009; Shimonishi et al. 2016b). This would suggest that both <sup>32</sup>SO(3<sub>3</sub>-2<sub>3</sub>) and <sup>32</sup>SO<sub>2</sub> lines are optically thin in the direction of ST16. The <sup>32</sup>S/<sup>34</sup>S ratio in the LMC sources is about one half compared with the solar neighborhood value ( $\sim 30$ , Chin et al. 1996), suggesting the overabundance of <sup>34</sup>S in the LMC.

The <sup>32</sup>S/<sup>33</sup>S ratios for SO and SO<sub>2</sub> (52 and 51) in ST16 are also, within the uncertainty, consistent with the previously reported <sup>32</sup>S/<sup>33</sup>S ratio of  $40 \pm 17$  estimated based on observations of the ST11 hot core (Shimonishi et al. 2016b). The <sup>32</sup>S/<sup>33</sup>S ratio of SO and SO<sub>2</sub> in the LMC is significantly lower than a typical solar neighborhood value by a factor of 3–4. As well as <sup>34</sup>S, <sup>33</sup>S is also overabundant in the LMC.

Sulfur is an  $\alpha$  element and massive stars mainly contribute to its nucleosynthesis. A theoretical model on the galactic chemical enrichment predicts the increasing trend of <sup>32</sup>S/<sup>33</sup>S, <sup>34</sup>S ratios according to the decreasing metallicity, because minor isotopes are synthesized from the seed of major isotopes as secondary elements in core-collapse supernovae, and thus more minor isotopes are produced at higher metallicity (Kobayashi et al. 2011). The trend is consistent with the observations of sulfur isotopes in our Galaxy, which report an increase of the <sup>32</sup>S/<sup>34</sup>S ratio from the Galactic inner part toward the solar neighborhood (see Figure 3 in Chin et al. 1996).

The sulfur isotope ratios in the LMC, however, significantly deviate from this trend. The observed <sup>32</sup>S/<sup>34</sup>S and <sup>32</sup>S/<sup>33</sup>S ratios in ST16 are lower than those of the model prediction at a half solar metallicity by a factor of two and four, respectively (see Table 3 in Kobayashi et al. 2011). The LMC's sulfur isotope ratio also deviates from the above-mentioned increasing trend of the <sup>32</sup>S/<sup>34</sup>S ratio from the Galactic inner part to the solar neighborhood. Interestingly, low <sup>32</sup>S/<sup>34</sup>S ratios are observed in millimeter molecular absorption line systems at the redshift of 0.68 and 0.89 (<sup>32</sup>S/<sup>34</sup>S  $\sim 9$  for CS/C<sup>34</sup>S and H<sub>2</sub>S/H<sub>2</sub> <sup>34</sup>S, Wallström et al. 2016). The reason for the characteristic isotope abundance ratios of sulfur in the LMC remains unexplained.

#### 5.6. Rotating Protostellar Envelope Traced by <sup>34</sup>SO and SO<sub>2</sub>

A sign of the rotating protostellar envelope is seen in the velocity maps of <sup>34</sup>SO and SO<sub>2</sub> (Figure 10). The maps are constructed based on the original Band 7 images without the beam restoration, where the beam size corresponds to  $0.090 \text{ pc} \times 0.076 \text{ pc}$  at the LMC. As shown in the figure, the east side of the core is redshifted and the west side is blueshifted, and the velocity separation is about 2–3 km s<sup>-1</sup>. The direction of the velocity separation is nearly perpendicular to the outflow axis, which is directed from northeast to southwest (see Section 5.7). This would support the idea that <sup>34</sup>SO and SO<sub>2</sub> are tracing the envelope rotation, rather than the outflow motion. Similar rotation motions are observed in Galactic high-mass protostellar objects (e.g., Beuther et al. 2007; Beltrán et al. 2011a, 2011b; Furuya et al. 2011; Zhang et al. 2019). The present result is the first detection of a rotating protostellar envelope outside our Galaxy.



**Table 6**  
Isotope Abundances of Sulfur

	ST16 <sup>a</sup>				ST11 <sup>b</sup>	N113 <sup>c</sup>	Solar Neighborhood <sup>d</sup>
	SO	SO <sub>2</sub>	CS	Weighted Mean <sup>e</sup>	SO <sub>2</sub>	CS	CS
<sup>32</sup> S/ <sup>34</sup> S	23 ± 8	15 ± 3	19 ± 3	17 ± 2	14 ± 3	~15	~30
<sup>32</sup> S/ <sup>33</sup> S	52 ± 5	51 ± 15	72 ± 18	53 ± 5	40 ± 17	<100	~180
<sup>34</sup> S/ <sup>33</sup> S	2 ± 1	3 ± 1	4 ± 1	3 ± 1	3 ± 2	<7	~6

**Notes.**

<sup>a</sup> This work.

<sup>b</sup> ALMA observations toward a LMC hot core, ST11 (Shimonishi et al. 2016b).

<sup>c</sup> Single-dish observations toward an LMC star-forming region, N113 (Wang et al. 2009).

<sup>d</sup> Chin et al. (1996).

<sup>e</sup> The weight is the inverse of the squared error value.

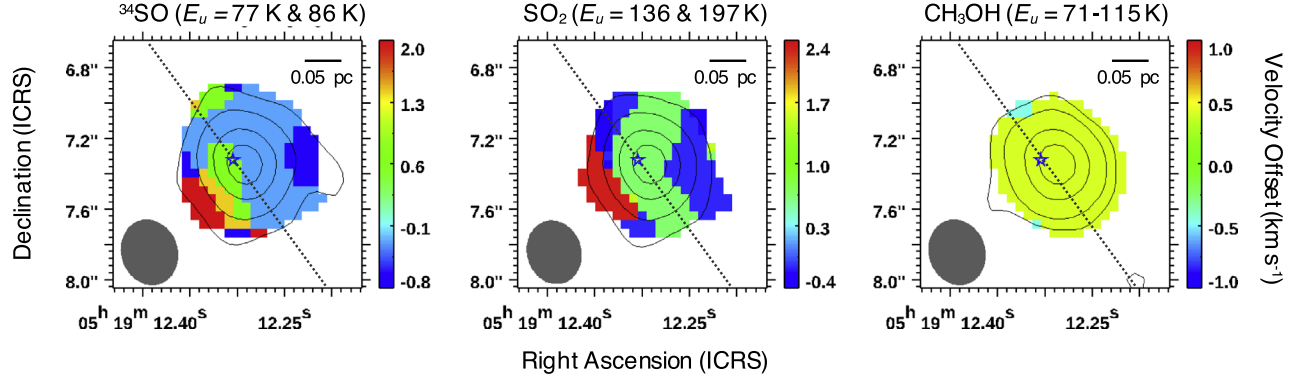


**Figure 10.** Velocity maps for <sup>34</sup>SO, SO<sub>2</sub>, and CH<sub>3</sub>OH. The color scale indicates the offset velocity relative to the systemic velocity of 264.5 km s<sup>-1</sup>. The contour represents the integrated intensity, where the level is 6%, 20%, 50%, and 80% of the peak value for <sup>34</sup>SO and SO<sub>2</sub>, while 10%, 20%, 50%, and 80% for CH<sub>3</sub>OH. The dotted line represents a possible outflow axis inferred from CCH and CN distribution (see Section 5.7). The maps are constructed by averaging the following Band 7 lines: <sup>34</sup>SO(*N<sub>J</sub>* = 8<sub>8</sub>–7<sub>7</sub> and 8<sub>9</sub>–7<sub>8</sub>), SO<sub>2</sub>(18<sub>4,14</sub>–18<sub>3,15</sub> and 14<sub>4,10</sub>–14<sub>3,11</sub>), CH<sub>3</sub>OH(7<sub>0</sub> E–6<sub>0</sub> E, 7<sub>–1</sub> E–6<sub>–1</sub> E, 7<sub>2</sub> A<sup>–</sup>–6<sub>2</sub> A<sup>–</sup>, 7<sub>3</sub> A<sup>+</sup>–6<sub>3</sub> A<sup>+</sup>, and 7<sub>–2</sub> E–6<sub>–2</sub> E). The blue open star represents the position of a high-mass YSO. The synthesized beam size is shown by the gray filled ellipse. See Section 5.6 for details.

SO does not show the rotation motion in the present data. This may be due to the contamination of a foreground cold component, because the strong SO lines (6<sub>6</sub>–5<sub>5</sub> and 8<sub>7</sub>–7<sub>6</sub>) are moderately optically thick (see Section 4.1), while the optically thin SO(3<sub>3</sub>–2<sub>3</sub>) is too weak to analyze the velocity structure.

Figure 10 also shows the velocity map for high-excitation CH<sub>3</sub>OH lines, but the rotating structure is not seen here, though these CH<sub>3</sub>OH trace a warm and dense region close to the protostar. This would indicate the different spatial distribution of CH<sub>3</sub>OH and <sup>34</sup>SO/SO<sub>2</sub> within the 0.1 pc scale region.

The different distributions of the sulfur-bearing species and CH<sub>3</sub>OH are also supported by their different line widths. Figure 11 compares the measured line FWHMs of the selected molecular species with their upper state energies. Blended lines and low-signal-to-noise ratio lines are excluded here. The figure shows that SO<sub>2</sub>, SO, and <sup>34</sup>SO have relatively large line widths (≥6 km s<sup>-1</sup>). A well-known shock tracer, SiO, also shows a broader line width. On the other, CH<sub>3</sub>OH lines show relatively narrow line widths (≤5 km s<sup>-1</sup> for *E<sub>u</sub>* < 150 K and ≤3 km s<sup>-1</sup> for *E<sub>u</sub>* > 150 K). Other molecules, H<sub>2</sub>CO, HNC, and OCS, which possibly trace a compact hot core region, show intermediate line widths between SO<sub>2</sub> and CH<sub>3</sub>OH. The relatively large line widths of SO and SO<sub>2</sub> would indicate that they arise from a more turbulent region compared with other molecular species. Given the similar line width of SiO and SO/SO<sub>2</sub>, such a turbulent region may be related to the shock.

We finally note that an infall motion is not seen in the present data, because we do not cover a fully optically thick

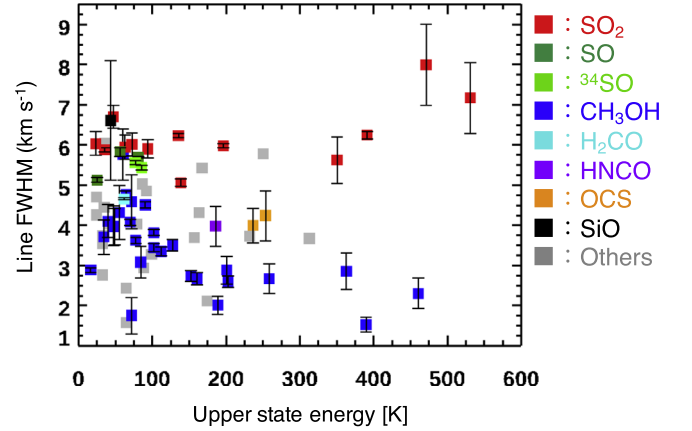


**Figure 11.** Line FWHMs vs. upper state energies. Blended lines and low-S/N lines are excluded. Molecular names are indicated by colors (SO<sub>2</sub>: red, SO: dark green, <sup>34</sup>SO: light green, CH<sub>3</sub>OH: blue, H<sub>2</sub>CO: cyan, HNC: purple, OCS: orange, SiO: black, others: gray).

molecular tracer in this work. Future higher-spatial-resolution multiline observations are required to further understand the dynamics of molecular gas associated with a low-metallicity massive protostellar envelope.

### 5.7. Outflow Cavity Structures Traced by CCH and CN

Spatial distributions of molecular radicals, CCH and CN, are similar to each other. In the LTE and optically thin case, the

expected intensity ratio of CCH lines at 349.33771 and 349.39928 GHz is 1.28 : 1.00, which is consistent with the observed integrated intensity ratio of  $(1.25 \pm 0.04) : (1.00 \pm 0.05)$  based on the data in Table 7, suggesting that the lines are optically thin. Similarly, for the same assumption, the expected ratio of CN lines at 340.03155, 340.03541, and 340.24777 GHz is 1.00 : 1.00 : 3.05, while the observed integrated intensity ratio is  $(1.00 \pm 0.10) : (1.11 \pm 0.11) : (2.75 \pm 0.08)$ , suggesting that they are nearly optically thin.

Obviously the CCH and CN distributions are not centered at the hot core position. They show emission peaks at the northeast and southwest direction from the hot core. Their distribution seems to trace bipolar outflow structures, originating from the protostar associated with the hot core. A well-collimated structure is seen particularly in the north direction. A width of the collimated structure is  $\sim 0.1$  pc, almost the same as the beam size. Given the early evolutionary stage of ST16, it is likely that molecular outflows are associated with the source.

CCH and CN emission are known to be bright in photodissociation regions (PDRs), and they are suggested to be a sensitive tracer of UV-irradiated regions (e.g., Fuente et al. 1993; Jansen et al. 1995; Rodriguez-Franco et al. 1998; Pety et al. 2017). The present characteristic distributions of CCH and CN presumably trace the PDR-like outflow cavity structure, which are irradiated by the UV light. According to the present dust continuum data, the visual extinction from the outer edge of the dust clump to the CCH/CN emission region is at least larger than 20 mag. Thus, a possible UV source for the photochemistry is a high-mass protostar located at the hot core position, rather than the external radiation field. Such a UV-irradiated outflow cavity is actually observed in Galactic star-forming regions via CCH emission (Zhang et al. 2018). The presence of high-velocity outflow gas needs to be tested by future high-spatial-resolution observations of strong and optically thick outflow tracers such as CO.

## 6. Summary

We present the results of  $0''.40$  ( $0.1$  pc)-scale submillimeter observations toward a high-mass YSO (ST16,  $L = 3 \times 10^5 L_{\odot}$ ) in the LMC with ALMA. As a result, a new hot molecular core is discovered in the LMC. The following conclusions are obtained in this work:

1. Molecular emission lines of  $\text{CH}_3\text{OH}$ ,  $\text{H}_2\text{CO}$ , CCH,  $\text{H}^{13}\text{CO}^+$ , CS,  $\text{C}^{34}\text{S}$ ,  $\text{C}^{33}\text{S}$ , SO,  $^{34}\text{SO}$ ,  $^{33}\text{SO}$ ,  $\text{SO}_2$ ,  $^{34}\text{SO}_2$ ,  $^{33}\text{SO}_2$ , OCS,  $\text{H}_2\text{CS}$ , CN, NO, HNC,  $\text{H}^{13}\text{CN}$ ,  $\text{CH}_3\text{CN}$ , and SiO are detected from the compact region ( $\sim 0.1$  pc) associated with a high-mass YSO. In total, we have detected 90 transitions, out of which, 30 lines are due to  $\text{CH}_3\text{OH}$ , and 27 lines are due to  $\text{SO}_2$  and its isotopologues. Complex organic molecules larger than  $\text{CH}_3\text{OH}$  are not detected.
2. Rotation analyses show that ST16 is associated with hot molecular gas ( $T_{\text{rot}} > 100$  K) as traced by  $\text{CH}_3\text{OH}$  and  $\text{SO}_2$ . The line of sight also contains warm ( $\sim 50$ – $60$  K) gas components traced by  $\text{CH}_3\text{OH}$ ,  $\text{SO}_2$ ,  $^{34}\text{SO}$ , OCS, and  $\text{CH}_3\text{CN}$ , in addition to extended and cold ( $\sim 25$  K) gas traced by SO.
3. The total gas column density toward ST16 is estimated by using several different methods (continuum analysis, SED analysis, and dust absorption band analysis). The estimated  $\text{H}_2$  column density is  $N_{\text{H}_2} = 5.6 \times 10^{23} \text{ cm}^{-2}$

(corresponds to  $A_V = 200$  mag). The average gas number density is estimated to be  $n_{\text{H}_2} = 3 \times 10^6 \text{ cm}^{-3}$ .

4. The nature of ST16, the compact source size, the high gas temperature, the high density, association with a high-mass YSO, and the presence of chemically rich molecular gas, strongly suggest that the source is associated with a hot molecular core.
5. Organic molecules show a large abundance variation in low-metallicity hot cores. There are currently two organic-poor hot cores (ST16 in this work and ST11 in Shimonishi et al. 2016b) and two organic-rich hot cores (N113 A1 and B3 in Sewilo et al. 2018) in the LMC. The different chemical history during the ice formation stage could contribute to the differentiation of organic-poor and organic-rich hot cores.
6. High-excitation  $\text{SO}_2$  lines will be a useful tracer of low-metallicity hot core chemistry. This is because (i)  $\text{SO}_2$  mainly originates from a hot core region, (ii) it is commonly seen in LMC hot cores, and (iii) its abundances in LMC hot cores roughly scale with the LMC's metallicity. This is remarkably in contrast to abundances of a classical hot core tracer,  $\text{CH}_3\text{OH}$ , which shows a large abundance variation in low-metallicity hot cores. CS and  $\text{H}_2\text{CS}$  are significantly less abundant in organic-poor hot cores.
7. Nitrogen-bearing molecules in ST16 are generally less abundant than those in Galactic hot cores. An exception is NO, whose abundance is comparable with Galactic values, despite the low elemental abundance. An overabundance of NO is also reported in the other LMC hot core (ST11).
8. Isotope abundance ratios of  $^{32}\text{S}$ ,  $^{33}\text{S}$ , and  $^{34}\text{S}$  in the ST16 hot core are presented. Based on SO,  $\text{SO}_2$ , and their isotopologues, we obtain  $^{32}\text{S}/^{34}\text{S} \sim 15$  and  $^{32}\text{S}/^{33}\text{S} \sim 40$ , which are lower than solar neighborhood values by a factor of 2 and 4.5, respectively. Both  $^{34}\text{S}$  and  $^{33}\text{S}$  are overabundant in the LMC.
9. A rotating protostellar envelope is, for the first time, detected outside our Galaxy via  $\text{SO}_2$  and  $^{34}\text{SO}$  lines.
10. CCH and CN show clearly different spatial distributions compared to other molecular lines. They seem to trace PDR-like cavity regions created by protostellar outflows.
11. Our astrochemical simulations for a low-metallicity hot core suggest that a large chemical diversity of organic molecules (e.g.,  $\text{CH}_3\text{OH}$ ) seen in LMC hot cores is related to the different physical condition at the initial stage of star formation. Particular molecular species that are mainly produced by high-temperature gas-phase chemistry in a hot core (e.g.,  $\text{SO}_2$ ) are likely to show a metallicity-scaled molecular abundance.

This paper makes use of the following ALMA data: ADS/JAO. ALMA#2016.1.00394.S and #2018.1.01366.S. ALMA is a partnership of ESO (representing its member states), NSF (USA) and NINS (Japan), together with NRC (Canada) and NSC and ASIAA (Taiwan) and KASI (Republic of Korea), in cooperation with the Republic of Chile. The Joint ALMA Observatory is operated by ESO, AUI/NRAO and NAOJ. This work has made extensive use of the Cologne Database for Molecular Spectroscopy and the molecular database of the Jet Propulsion Laboratory. We use data obtained by IRSF/SIRIUS, VLT/ISAAC, AKARI, Spitzer, and Herschel. We are grateful to all the members who contributed to these projects. T.S. is supported by a Grant-in-Aid for Scientific Research on Innovative Areas (19H05067) and

Leading Initiative for Excellent Young Researchers, MEXT, Japan. A.D. acknowledges the ISRO RESPOND program (grant No. ISRO/RES/2/402/16-17) and Grant-In-Aid from the Higher Education Department of the Government of West Bengal. K.E.I.T. acknowledges support from NAOJ ALMA Scientific Research grant No. 2017-05A and JSPS KAKENHI grant No. JP19K14760. Y.A. acknowledges support from NAOJ ALMA Scientific Research grant No. 2019-13B and Grant-in-Aid for Scientific Research (S) grant No. 18H05222. Y.N. is supported by NAOJ ALMA Scientific Research grant No. 2017-06B and JSPS

KAKENHI grant No. JP18K13577. Finally, we would like to thank an anonymous referee for careful reading and useful comments.

## Appendix A Measured Line Parameters

Tables 7–9 summarize observed line parameters (see Section 3.1 for details).

**Table 7**  
Line Parameters

Molecule	Transition	$E_u$ (K)	Frequency (GHz)	$T_b$ (K)	$\Delta V$ (km s <sup>-1</sup> )	$\int T_b dV$ (K km s <sup>-1</sup> )	$V_{LSR}$ (km s <sup>-1</sup> )	rms (K)	Note
CCH	$N = 4-3, J = \frac{9}{2}-\frac{7}{2}, F = 5-4$	42	349.33771	$1.43 \pm 0.02$	4.0	$6.14 \pm 0.22$	263.9	0.06	(1)
CCH	$N = 4-3, J = \frac{7}{2}-\frac{5}{2}, F = 4-3$	42	349.39928	$1.15 \pm 0.02$	4.0	$4.93 \pm 0.22$	264.0	0.06	(2)
H <sub>2</sub> CO	$5_{1,5}-4_{1,4}$	62	351.76864	$6.63 \pm 0.03$	4.7	$32.83 \pm 0.31$	264.5	0.06	...
H <sup>13</sup> CO <sup>+</sup>	$3-2$	25	260.25534	$3.21 \pm 0.14$	4.7	$16.00 \pm 1.50$	264.7	0.29	...
CS	$5-4$	35	244.93556	$8.55 \pm 0.16$	4.4	$40.43 \pm 1.59$	264.4	0.30	...
C <sup>34</sup> S	$7-6$	65	337.39646	$0.88 \pm 0.03$	2.4	$2.28 \pm 0.14$	264.3	0.06	...
C <sup>33</sup> S	$5-4$	35	242.91361	<0.60	...	<2.6	...	0.30	...
C <sup>33</sup> S	$7-6$	65	340.05257	$0.36 \pm 0.03$	<2	$0.60 \pm 0.10$	264.5	0.06	...
SO	$N_J = 6_6-5_5$	56	258.25583	$9.73 \pm 0.16$	5.8	$60.26 \pm 2.16$	264.8	0.29	...
SO	$N_J = 3_3-2_3$	26	339.34146	$2.90 \pm 0.03$	5.1	$15.79 \pm 0.37$	265.0	0.06	...
SO	$N_J = 8_7-7_6$	81	340.71416	$10.84 \pm 0.03$	5.7	$65.66 \pm 0.42$	264.7	0.06	...
<sup>34</sup> SO	$N_J = 8_8-7_7$	86	337.58015	$2.90 \pm 0.03$	5.4	$16.76 \pm 0.32$	264.9	0.06	...
<sup>34</sup> SO	$N_J = 3_3-2_3$	25	337.89225	$0.20 \pm 0.02$	3.1	$0.67 \pm 0.17$	265.2	0.06	...
<sup>34</sup> SO	$N_J = 8_9-7_8$	77	339.85727	$3.19 \pm 0.02$	5.5	$18.82 \pm 0.31$	265.0	0.06	...
<sup>33</sup> SO	$N_J = 6_7-5_6$	47	259.28403	$1.48 \pm 0.58$	...	$6.14 \pm 0.76$	...	0.29	(3) (4)
<sup>33</sup> SO	$N_J = 8_8-7_7$	87	340.83964	$1.43 \pm 0.03$	5.0	$7.66 \pm 0.37$	266.0	0.06	(5)
H <sub>2</sub> CS	$7_{1,6}-6_{1,5}$	60	244.04850	<0.60	...	<2.6	...	0.30	...
H <sub>2</sub> CS	$10_{1,10}-9_{1,9}$	102	338.08319	$0.25 \pm 0.02$	3.4	$0.92 \pm 0.19$	264.7	0.06	...
OCS	$20-19$	123	243.21804	$0.89 \pm 0.16$	5.7	$5.40 \pm 1.98$	265.3	0.30	†
OCS	$28-27$	237	340.44927	$0.27 \pm 0.02$	4.0	$1.13 \pm 0.22$	263.1	0.06	...
OCS	$29-28$	254	352.59957	$0.22 \pm 0.02$	4.2	$1.00 \pm 0.23$	264.4	0.06	...
CN	$N = 3-2, J = \frac{5}{2}-\frac{3}{2}, F = \frac{7}{2}-\frac{5}{2}$	33	340.03155	$0.96 \pm 0.03$	2.8	$2.82 \pm 0.28$	265.0	0.06	(6)
CN	$N = 3-2, J = \frac{5}{2}-\frac{3}{2}, F = \frac{5}{2}-\frac{3}{2}$	33	340.03541	$0.83 \pm 0.02$	3.5	$3.12 \pm 0.32$	264.8	0.06	(7)
CN	$N = 3-2, J = \frac{7}{2}-\frac{5}{2}, F = \frac{9}{2}-\frac{7}{2}$	33	340.24777	$1.95 \pm 0.03$	3.7	$7.75 \pm 0.22$	264.4	0.06	(8)
H <sup>13</sup> CN	$3-2$	25	259.01180	$1.27 \pm 0.13$	4.2	$5.76 \pm 1.31$	265.0	0.29	...
NO	$J = \frac{7}{2}-\frac{5}{2}, \Omega = \frac{1}{2}, F = \frac{9}{2}-\frac{7}{2} +$	36	350.68949	<0.90	...	<3.8	...	0.06	(9) (10)
NO	$J = \frac{7}{2}-\frac{5}{2}, \Omega = \frac{1}{2}, F = \frac{5}{2}-\frac{3}{2} +$	36	350.69477	<0.70	...	<3.0	...	0.06	(9)
NO	$J = \frac{7}{2}-\frac{5}{2}, \Omega = \frac{1}{2}, F = \frac{9}{2}-\frac{7}{2} -$	36	351.04352	$0.33 \pm 0.02$	6.0	$2.12 \pm 0.40$	264.8	0.06	...
NO	$J = \frac{7}{2}-\frac{5}{2}, \Omega = \frac{1}{2}, F = \frac{7}{2}-\frac{5}{2} -$	36	351.05171	$0.82 \pm 0.02$	3.3	$2.87 \pm 0.21$	264.6	0.06	(11)
HNCO	$11_{0,11}-10_{0,10}$	70	241.77403	<1.00	...	<4.3	...	0.30	...
HNCO	$16_{1,16}-15_{1,15}$	186	350.33306	$0.21 \pm 0.02$	4.0	$0.89 \pm 0.20$	264.9	0.06	...
HNCO	$16_{2,15}-15_{2,14}$	314	351.53780	<0.12	...	<0.5	...	0.06	...
HNCO	$16_{2,14}-15_{2,13}$	314	351.55157	<0.12	...	<0.5	...	0.06	...
HNCO	$16_{0,16}-15_{0,15}$	143	351.63326	$0.58 \pm 0.03$	4.0	$2.50 \pm 0.26$	264.3	0.06	(12)
CH <sub>3</sub> CN	$14_3-13_{-3}$	157	257.48279	$1.18 \pm 0.14$	3.7	$4.63 \pm 1.20$	265.6	0.29	(13)
CH <sub>3</sub> CN	$14_2-13_2$	121	257.50756	$0.69 \pm 0.12$	3.5	$2.55 \pm 0.99$	263.9	0.29	<sup>a</sup> (13)
CH <sub>3</sub> CN	$14_1-13_1$	100	257.52243	<0.9	...	<3.8	...	0.29	(14)
CH <sub>3</sub> CN	$14_0-13_0$	93	257.52738	<0.9	...	<3.8	...	0.29	...
CH <sub>3</sub> CN	$19_4-18_4$	282	349.34634	<0.12	...	<0.5	...	0.06	(13)
CH <sub>3</sub> CN	$19_3-18_{-3}$	232	349.39330	$0.27 \pm 0.02$	3.7	$1.08 \pm 0.20$	264.3	0.06	(14) (15)
CH <sub>3</sub> CN	$19_2-18_2$	196	349.42685	<0.25	...	<1.1	...	0.06	(13)
CH <sub>3</sub> CN	$19_1-18_1$	175	349.44699	$0.49 \pm 0.02$	2.1	$1.11 \pm 0.14$	264.8	0.06	(13)
CH <sub>3</sub> CN	$19_0-18_0$	168	349.45370	$0.22 \pm 0.02$	5.4	$1.25 \pm 0.28$	264.0	0.06	...
HC <sub>3</sub> N	$27-26$	165	245.60632	<0.60	...	<2.6	...	0.30	...
SiO	$6-5$	44	260.51801	$0.71 \pm 0.11$	6.6	$5.02 \pm 1.90$	265.6	0.29	†
c-C <sub>3</sub> H <sub>2</sub>	$5_{3,2}-4_{4,1}$	45	260.47975	<0.58	...	<2.5	...	0.29	...
HDO	$2-1$	95	241.56155	<0.60	...	<2.6	...	0.30	...
C <sub>2</sub> H <sub>5</sub> OH	$6_{5,2}-5_{4,1}$	49	340.18925	<0.12	...	<0.5	...	0.06	(16)
C <sub>2</sub> H <sub>5</sub> OH	$20_{2,19}-19_{1,18}$	179	350.53435	<0.12	...	<0.5	...	0.06	...



**Table 7**  
(Continued)

Molecule	Transition	$E_u$ (K)	Frequency (GHz)	$T_b$ (K)	$\Delta V$ (km s <sup>-1</sup> )	$\int T_b dV$ (K km s <sup>-1</sup> )	$V_{LSR}$ (km s <sup>-1</sup> )	rms (K)	Note
C <sub>2</sub> H <sub>5</sub> CN	16 <sub>5,12</sub> –15 <sub>4,11</sub>	86	351.53144	<0.12	...	<0.5	...	0.06	...
CH <sub>3</sub> OCH <sub>3</sub>	19 <sub>1,18</sub> –18 <sub>2,17</sub> EE	176	339.49153	<0.12	...	<0.5	...	0.06	(17)
HCOOCH <sub>3</sub>	28 <sub>5,24</sub> –27 <sub>5,23</sub> E	257	340.74199	<0.12	...	<0.5	...	0.06	...
<i>trans</i> -HCOOH	15 <sub>3,13</sub> –14 <sub>3,12</sub>	158	338.20186	<0.12	...	<0.5	...	0.06	...

**Notes.** Uncertainties and upper limits are at the  $2\sigma$  level and do not include systematic errors due to continuum subtraction. Upper limits are estimated by assuming  $\Delta V = 4$  km s<sup>-1</sup>.

<sup>a</sup> Tentative detection. (1) Blend with  $F = 4-3$ . (2) Blend with  $F = 3-2$ . (3) Blend of four hyperfine components. (4) The integrated intensity is calculated by directly integrating the spectrum. (5) Blend of seven hyperfine components. (6) Partially blended with CN at 340.03541 GHz. (7) Blend with  $F = \frac{3}{2}-\frac{1}{2}$ . (8) Blend with  $F = \frac{7}{2}-\frac{5}{2}$  and  $\frac{5}{2}-\frac{3}{2}$ . (9) Blend with CH<sub>3</sub>OH (4<sub>0</sub> E–3<sub>-1</sub> E). (10) Blend with  $F = \frac{7}{2}-\frac{5}{2}^+$ . (11) Blend with  $F = \frac{5}{2}-\frac{3}{2}^-$ . (12) Possible blend with <sup>33</sup>SO<sub>2</sub> (5<sub>4,2</sub>–5<sub>3,3</sub>). (13) Blend of two hyperfine components. (14) Blend of four hyperfine components. (15) Partially blended with CCH at 349.39928 GHz. (16) Blend with 6<sub>5,1</sub>–5<sub>4,2</sub>. (17) Blend with AA, AE, and EA transitions.

**Table 8**  
Line Parameters (CH<sub>3</sub>OH)

Molecule	Transition	$E_u$ (K)	Frequency (GHz)	$T_b$ (K)	$\Delta V$ (km s <sup>-1</sup> )	$\int T_b dV$ (K km s <sup>-1</sup> )	$V_{LSR}$ (km s <sup>-1</sup> )	rms (K)	Note
CH <sub>3</sub> OH	5 <sub>0</sub> E–4 <sub>0</sub> E	48	241.70016	1.40 ± 0.12	4.0	5.91 ± 1.27	263.6	0.30	...
CH <sub>3</sub> OH	5 <sub>-1</sub> E–4 <sub>-1</sub> E	40	241.76723	1.58 ± 0.13	4.1	6.89 ± 1.25	264.2	0.30	...
CH <sub>3</sub> OH	5 <sub>0</sub> A <sup>+</sup> –4 <sub>0</sub> A <sup>+</sup>	35	241.79135	1.44 ± 0.14	3.7	5.67 ± 1.23	264.8	0.30	...
CH <sub>3</sub> OH	5 <sub>-4</sub> E–4 <sub>-4</sub> E	123	241.81325	<0.60	...	<2.6	...	0.30	...
CH <sub>3</sub> OH	5 <sub>4</sub> E–4 <sub>4</sub> E	131	241.82963	<0.60	...	<2.6	...	0.30	...
CH <sub>3</sub> OH	5 <sub>3</sub> A <sup>+</sup> –4 <sub>3</sub> A <sup>+</sup>	85	241.83272	1.53 ± 0.14	3.1	5.02 ± 1.11	264.4	0.30	(1)
CH <sub>3</sub> OH	5 <sub>2</sub> A <sup>-</sup> –4 <sub>2</sub> A <sup>-</sup>	73	241.84228	1.11 ± 0.14	4.6	5.39 ± 1.47	264.3	0.30	(2)
CH <sub>3</sub> OH	5 <sub>-3</sub> E–4 <sub>-3</sub> E	98	241.85230	<0.60	...	<2.6	...	0.30	...
CH <sub>3</sub> OH	5 <sub>1</sub> E–4 <sub>1</sub> E	56	241.87903	1.05 ± 0.14	4.3	4.80 ± 1.38	264.8	0.30	...
CH <sub>3</sub> OH	5 <sub>2</sub> A <sup>+</sup> –4 <sub>2</sub> A <sup>+</sup>	73	241.88767	0.86 ± 0.15	1.7	1.60 ± 0.70	264.3	0.30	<sup>a</sup>
CH <sub>3</sub> OH	5 <sub>-2</sub> E–4 <sub>-2</sub> E	61	241.90415	1.48 ± 0.13	5.8	9.04 ± 1.81	265.6	0.30	(3)
CH <sub>3</sub> OH	14 <sub>-1</sub> E–13 <sub>-2</sub> E	249	242.44608	<0.60	...	<2.6	...	0.30	...
CH <sub>3</sub> OH	5 <sub>1</sub> A <sup>-</sup> –4 <sub>1</sub> A <sup>-</sup>	50	243.91579	1.45 ± 0.12	4.0	6.10 ± 1.20	264.3	0.30	...
CH <sub>3</sub> OH	9 <sub>1</sub> E–8 <sub>0</sub> E, $\nu_t = 1$	396	244.33798	<0.60	...	<2.6	...	0.30	...
CH <sub>3</sub> OH	7 <sub>3</sub> E–6 <sub>3</sub> E, $\nu_t = 1$	482	337.51914	<0.12	...	<0.5	...	0.06	...
CH <sub>3</sub> OH	7 <sub>-2</sub> E–6 <sub>-2</sub> E, $\nu_t = 1$	429	337.60529	<0.12	...	<0.5	...	0.06	...
CH <sub>3</sub> OH	7 <sub>2</sub> A <sup>+</sup> –6 <sub>2</sub> A <sup>+</sup> , $\nu_t = 1$	363	337.62575	0.19 ± 0.02	2.8	0.58 ± 0.16	263.2	0.06	<sup>a</sup>
CH <sub>3</sub> OH	7 <sub>2</sub> A <sup>-</sup> –6 <sub>2</sub> A <sup>-</sup> , $\nu_t = 1$	364	337.63575	<0.12	...	<0.5	...	0.06	...
CH <sub>3</sub> OH	7 <sub>0</sub> E–6 <sub>0</sub> E, $\nu_t = 1$	365	337.64391	0.27 ± 0.02	4.6	1.32 ± 0.25	264.9	0.06	(4)
CH <sub>3</sub> OH	7 <sub>3</sub> A <sup>+</sup> –6 <sub>3</sub> A <sup>+</sup> , $\nu_t = 1$	461	337.65520	0.18 ± 0.03	2.3	0.45 ± 0.14	264.9	0.06	<sup>a</sup> (5)
CH <sub>3</sub> OH	7 <sub>-1</sub> E–6 <sub>-1</sub> E, $\nu_t = 1$	478	337.70757	<0.12	...	<0.5	...	0.06	...
CH <sub>3</sub> OH	7 <sub>0</sub> A <sup>+</sup> –6 <sub>0</sub> A <sup>+</sup> , $\nu_t = 1$	488	337.74883	<0.12	...	<0.5	...	0.06	...
CH <sub>3</sub> OH	7 <sub>1</sub> A <sup>-</sup> –6 <sub>1</sub> A <sup>-</sup> , $\nu_t = 1$	390	337.96944	0.24 ± 0.03	1.5	0.38 ± 0.09	265.0	0.06	...
CH <sub>3</sub> OH	7 <sub>0</sub> E–6 <sub>0</sub> E	78	338.12449	1.44 ± 0.03	3.6	5.54 ± 0.23	264.6	0.06	...
CH <sub>3</sub> OH	7 <sub>-1</sub> E–6 <sub>-1</sub> E	71	338.34459	1.67 ± 0.03	4.1	7.25 ± 0.25	264.3	0.06	...
CH <sub>3</sub> OH	7 <sub>6</sub> E–6 <sub>6</sub> E	244	338.40461	<0.40	...	<1.7	...	0.06	...
CH <sub>3</sub> OH	7 <sub>0</sub> A <sup>+</sup> –6 <sub>0</sub> A <sup>+</sup>	65	338.40870	1.73 ± 0.03	4.8	8.75 ± 0.28	264.7	0.06	(6)
CH <sub>3</sub> OH	7 <sub>-6</sub> E–6 <sub>-6</sub> E	254	338.43097	<0.12	...	<0.5	...	0.06	...
CH <sub>3</sub> OH	7 <sub>6</sub> A <sup>+</sup> –6 <sub>6</sub> A <sup>+</sup>	259	338.44237	0.20 ± 0.02	2.7	0.57 ± 0.14	265.3	0.06	(7)
CH <sub>3</sub> OH	7 <sub>-5</sub> E–6 <sub>-5</sub> E	189	338.45654	0.58 ± 0.03	2.0	1.25 ± 0.20	264.5	0.06	...
CH <sub>3</sub> OH	7 <sub>5</sub> E–6 <sub>5</sub> E	201	338.47523	0.37 ± 0.03	2.9	1.12 ± 0.22	265.2	0.06	...
CH <sub>3</sub> OH	7 <sub>5</sub> A <sup>+</sup> –6 <sub>5</sub> A <sup>+</sup>	203	338.48632	0.69 ± 0.03	2.6	1.89 ± 0.18	264.7	0.06	(8)
CH <sub>3</sub> OH	7 <sub>-4</sub> E–6 <sub>-4</sub> E	153	338.50407	1.77 ± 0.02	2.7	2.24 ± 0.18	264.5	0.06	...
CH <sub>3</sub> OH	7 <sub>2</sub> A <sup>-</sup> –6 <sub>2</sub> A <sup>-</sup>	103	338.51285	0.63 ± 0.03	3.8	6.63 ± 0.23	264.6	0.06	(9)
CH <sub>3</sub> OH	7 <sub>4</sub> E–6 <sub>4</sub> E	161	338.53026	0.62 ± 0.03	2.7	1.75 ± 0.18	264.5	0.06	...
CH <sub>3</sub> OH	7 <sub>3</sub> A <sup>+</sup> –6 <sub>3</sub> A <sup>+</sup>	115	338.54083	1.50 ± 0.02	5.4	8.60 ± 0.30	263.5	0.06	(10)
CH <sub>3</sub> OH	7 <sub>-3</sub> E–6 <sub>-3</sub> E	128	338.55996	0.78 ± 0.03	3.5	2.89 ± 0.21	264.5	0.06	...
CH <sub>3</sub> OH	7 <sub>3</sub> E–6 <sub>3</sub> E	113	338.58322	0.90 ± 0.03	3.3	3.21 ± 0.20	264.8	0.06	...
CH <sub>3</sub> OH	7 <sub>2</sub> A <sup>+</sup> –6 <sub>2</sub> A <sup>+</sup>	103	338.63980	1.15 ± 0.03	3.4	4.20 ± 0.22	264.5	0.06	...
CH <sub>3</sub> OH	7 <sub>-2</sub> E–6 <sub>-2</sub> E	91	338.72290	1.99 ± 0.03	4.5	9.52 ± 0.28	265.0	0.06	(11)
CH <sub>3</sub> OH	2 <sub>2</sub> A <sup>+</sup> –3 <sub>1</sub> A <sup>+</sup>	45	340.14114	<0.12	...	<0.5	...	0.06	...
CH <sub>3</sub> OH	16 <sub>6</sub> A <sup>-</sup> –17 <sub>5</sub> A <sup>-</sup>	509	340.39366	<0.12	...	<0.5	...	0.06	(12)
CH <sub>3</sub> OH	11 <sub>1</sub> E–10 <sub>0</sub> E, $\nu_t = 1$	444	340.68397	<0.12	...	<0.5	...	0.06	...
CH <sub>3</sub> OH	4 <sub>0</sub> E–3 <sub>-1</sub> E	36	350.68766	1.66 ± 0.03	3.0	5.26 ± 0.31	264.4	0.06	(13)

**Table 8**  
(Continued)

Molecule	Transition	$E_u$ (K)	Frequency (GHz)	$T_b$ (K)	$\Delta V$ (km s <sup>-1</sup> )	$\int T_b dV$ (K km s <sup>-1</sup> )	$V_{LSR}$ (km s <sup>-1</sup> )	rms (K)	Note
CH <sub>3</sub> OH	1 <sub>1</sub> A <sup>+</sup> -0 <sub>0</sub> A <sup>+</sup>	17	350.90510	1.86 ± 0.02	2.9	5.68 ± 0.20	264.6	0.06	...
CH <sub>3</sub> OH	9 <sub>5</sub> E-10 <sub>4</sub> E	241	351.23648	<0.12	...	<0.5	...	0.06	...

**Notes.** Uncertainties and upper limits are at the 2 $\sigma$  level and do not include systematic errors due to continuum subtraction. Upper limits are estimated assuming  $\Delta V = 4$  km s<sup>-1</sup>.

<sup>a</sup> Tentative detection. (1) Blend with 5<sub>3</sub> A<sup>-</sup>-4<sub>3</sub> A<sup>-</sup>. (2) Blend with 5<sub>3</sub>E-4<sub>3</sub>E. (3) Blend with 5<sub>2</sub> E-4<sub>2</sub> E. (4) Blend with 7<sub>1</sub> E-6<sub>1</sub> E. (5) Blend with 7<sub>3</sub> A<sup>-</sup>-6<sub>3</sub> A<sup>-</sup>. (6) Possible blend with 7<sub>6</sub> E-6<sub>6</sub> E. (7) Blend with 7<sub>6</sub> A<sup>-</sup>-6<sub>6</sub> A<sup>-</sup>. (8) Blend with 7<sub>5</sub> A<sup>-</sup>-6<sub>5</sub> A<sup>-</sup>. (9) Blend with 7<sub>4</sub> A<sup>-</sup>-6<sub>4</sub> A<sup>-</sup> and 7<sub>4</sub> A<sup>+</sup>-6<sub>4</sub> A<sup>+</sup>. (10) Blend with 7<sub>3</sub> A<sup>-</sup>-6<sub>3</sub> A<sup>-</sup>. (11) Blend with 7<sub>+</sub>2 E-6<sub>+</sub>2 E. (12) Blend with 16<sub>6</sub> A<sup>+</sup>-17<sub>5</sub> A<sup>+</sup>. (13) Partially blended with NO at 350.68949 and 350.69477 GHz.

**Table 9**  
Line Parameters (SO<sub>2</sub>, <sup>34</sup>SO<sub>2</sub>, and <sup>33</sup>SO<sub>2</sub>)

Molecule	Transition	$E_u$ (K)	Frequency (GHz)	$T_b$ (K)	$\Delta V$ (km s <sup>-1</sup> )	$\int T_b dV$ (K km s <sup>-1</sup> )	$V_{LSR}$ (km s <sup>-1</sup> )	rms (K)	Note
SO <sub>2</sub>	5 <sub>2,4</sub> -4 <sub>1,3</sub>	24	241.61580	3.41 ± 0.14	6.0	21.88 ± 1.98	264.8	0.30	...
SO <sub>2</sub>	5 <sub>4,2</sub> -6 <sub>3,3</sub>	53	243.08765	<0.60	...	<2.6	...	0.30	...
SO <sub>2</sub>	26 <sub>8,18</sub> -27 <sub>7,21</sub>	480	243.24543	<0.60	...	<2.6	...	0.30	...
SO <sub>2</sub>	14 <sub>0,14</sub> -13 <sub>1,13</sub>	94	244.25422	4.18 ± 0.14	5.9	26.26 ± 1.94	265.0	0.30	...
SO <sub>2</sub>	26 <sub>3,23</sub> -25 <sub>4,22</sub>	351	245.33923	1.60 ± 0.14	5.6	9.54 ± 1.81	264.4	0.30	...
SO <sub>2</sub>	10 <sub>3,7</sub> -10 <sub>2,8</sub>	73	245.56342	3.43 ± 0.14	6.0	21.93 ± 1.96	265.1	0.30	...
SO <sub>2</sub>	7 <sub>3,5</sub> -7 <sub>2,6</sub>	48	257.09997	3.59 ± 0.12	6.7	25.55 ± 1.95	264.9	0.29	...
SO <sub>2</sub>	32 <sub>4,28</sub> -32 <sub>3,29</sub>	531	258.38872	1.23 ± 0.12	7.2	9.37 ± 2.07	264.4	0.29	...
SO <sub>2</sub>	20 <sub>7,13</sub> -21 <sub>6,16</sub>	313	258.66697	1.08 ± 0.13	3.7	4.22 ± 1.12	265.4	0.29	...
SO <sub>2</sub>	9 <sub>3,7</sub> -9 <sub>2,8</sub>	63	258.94220	3.10 ± 0.14	5.9	19.61 ± 1.84	265.0	0.29	...
SO <sub>2</sub>	30 <sub>4,26</sub> -30 <sub>3,27</sub>	472	259.59945	1.27 ± 0.12	8.0	10.79 ± 2.35	263.9	0.29	...
SO <sub>2</sub>	18 <sub>4,14</sub> -18 <sub>3,15</sub>	197	338.30599	3.30 ± 0.02	6.0	20.98 ± 0.32	264.9	0.06	...
SO <sub>2</sub>	20 <sub>1,19</sub> -19 <sub>2,18</sub>	199	338.61181	4.24 ± 0.03	6.6	29.80 ± 0.38	264.3	0.06	(1)
SO <sub>2</sub>	39 <sub>6,34</sub> -40 <sub>3,37</sub>	808	339.25959	<0.12	...	<0.5	...	0.06	...
SO <sub>2</sub>	28 <sub>2,26</sub> -28 <sub>1,27</sub>	392	340.31641	2.01 ± 0.03	6.2	13.33 ± 0.35	264.6	0.06	...
SO <sub>2</sub>	31 <sub>10,22</sub> -32 <sub>9,23</sub>	701	349.22706	0.17 ± 0.02	6.6	1.23 ± 0.34	263.1	0.04	(2)
SO <sub>2</sub>	10 <sub>6,4</sub> -11 <sub>5,7</sub>	139	350.86276	1.81 ± 0.03	5.1	9.73 ± 0.32	264.6	0.06	...
SO <sub>2</sub>	5 <sub>3,3</sub> -4 <sub>2,2</sub>	36	351.25722	4.03 ± 0.03	5.9	25.17 ± 0.37	265.0	0.06	...
SO <sub>2</sub>	14 <sub>4,10</sub> -14 <sub>3,11</sub>	136	351.87387	3.40 ± 0.03	6.2	22.49 ± 0.38	264.9	0.06	...
<sup>34</sup> SO <sub>2</sub>	14 <sub>0,14</sub> -13 <sub>1,13</sub>	94	244.48152	0.55 ± 0.13	5.9	3.49 ± 1.90	264.3	0.21	<sup>a</sup> (2)
<sup>34</sup> SO <sub>2</sub>	34 <sub>5,29</sub> -34 <sub>4,30</sub>	609	337.87269	<0.12	...	<0.5	...	0.06	...
<sup>34</sup> SO <sub>2</sub>	13 <sub>2,12</sub> -12 <sub>1,11</sub>	92	338.32036	0.85 ± 0.02	4.8	4.38 ± 0.41	265.1	0.06	...
<sup>34</sup> SO <sub>2</sub>	14 <sub>4,10</sub> -14 <sub>3,11</sub>	134	338.78569	0.78 ± 0.03	4.0	3.34 ± 0.23	264.6	0.06	...
<sup>34</sup> SO <sub>2</sub>	34 <sub>4,30</sub> -33 <sub>5,29</sub>	593	350.61933	<0.12	...	<0.5	...	0.06	...
<sup>34</sup> SO <sub>2</sub>	21 <sub>4,18</sub> -21 <sub>3,19</sub>	250	352.08292	0.27 ± 0.02	5.8	1.68 ± 0.30	265.0	0.06	...
<sup>33</sup> SO <sub>2</sub>	16 <sub>4,12</sub> -16 <sub>3,13</sub>	164	339.48232	0.21 ± 0.02	4.3	0.99 ± 0.22	263.9	0.06	(3)
<sup>33</sup> SO <sub>2</sub>	20 <sub>1,19</sub> -19 <sub>2,18</sub>	199	340.52818	0.20 ± 0.12	6.0	0.73 ± 0.16	264.8	0.06	<sup>a</sup> (4) (5)
<sup>33</sup> SO <sub>2</sub>	10 <sub>4,6</sub> -10 <sub>3,7</sub>	89	350.30323	0.22 ± 0.02	2.9	0.69 ± 0.16	265.1	0.06	(3)
<sup>33</sup> SO <sub>2</sub>	13 <sub>4,10</sub> -13 <sub>3,11</sub>	122	350.78808	<0.2	...	<1.1	...	0.06	(3)
<sup>33</sup> SO <sub>2</sub>	11 <sub>4,8</sub> -11 <sub>3,9</sub>	99	350.99508	0.29 ± 0.02	3.3	1.01 ± 0.17	265.0	0.06	(3)
<sup>33</sup> SO <sub>2</sub>	8 <sub>4,4</sub> -8 <sub>3,5</sub>	72	351.17796	0.16 ± 0.02	5.1	0.88 ± 0.26	263.9	0.06	<sup>a</sup> (3)
<sup>33</sup> SO <sub>2</sub>	9 <sub>4,6</sub> -9 <sub>3,7</sub>	80	351.28137	0.27 ± 0.02	4.0	1.15 ± 0.21	265.1	0.06	(3)
<sup>33</sup> SO <sub>2</sub>	7 <sub>4,4</sub> -7 <sub>3,5</sub>	64	351.50890	<0.12	...	<0.5	...	0.06	(3)
<sup>33</sup> SO <sub>2</sub>	6 <sub>4,2</sub> -6 <sub>3,3</sub>	58	351.54238	0.21 ± 0.03	1.9	0.42 ± 0.14	265.2	0.06	(3)
<sup>33</sup> SO <sub>2</sub>	5 <sub>4,2</sub> -5 <sub>3,3</sub>	52	351.63513	<0.20	...	<0.9	...	0.06	(3)
<sup>33</sup> SO <sub>2</sub>	4 <sub>4,0</sub> -4 <sub>3,1</sub>	48	351.66122	<0.12	...	<0.5	...	0.06	(3)
<sup>33</sup> SO <sub>2</sub>	17 <sub>4,14</sub> -17 <sub>3,15</sub>	179	351.74492	<0.20	...	<0.9	...	0.06	(6)

**Notes.** Uncertainties and upper limits are at the 2 $\sigma$  level and do not include systematic errors due to continuum subtraction. Upper limits are estimated assuming  $\Delta V = 4$  km s<sup>-1</sup>.

<sup>a</sup> Tentative detection. (1) Possible blend with CH<sub>3</sub>OH(7<sub>1</sub>E-6<sub>1</sub>E). (2) Two channels averaged upon fitting. (3) Blend of ten hyperfine components. (4) Blend of seven hyperfine components. (5) The integrated intensity is calculated by directly integrating the spectrum. (6) Blend of four hyperfine components.

## Appendix B Fitted Spectra

Figures 12–14 show observed spectra and the results of the line fitting (see Section 3.1 for details).

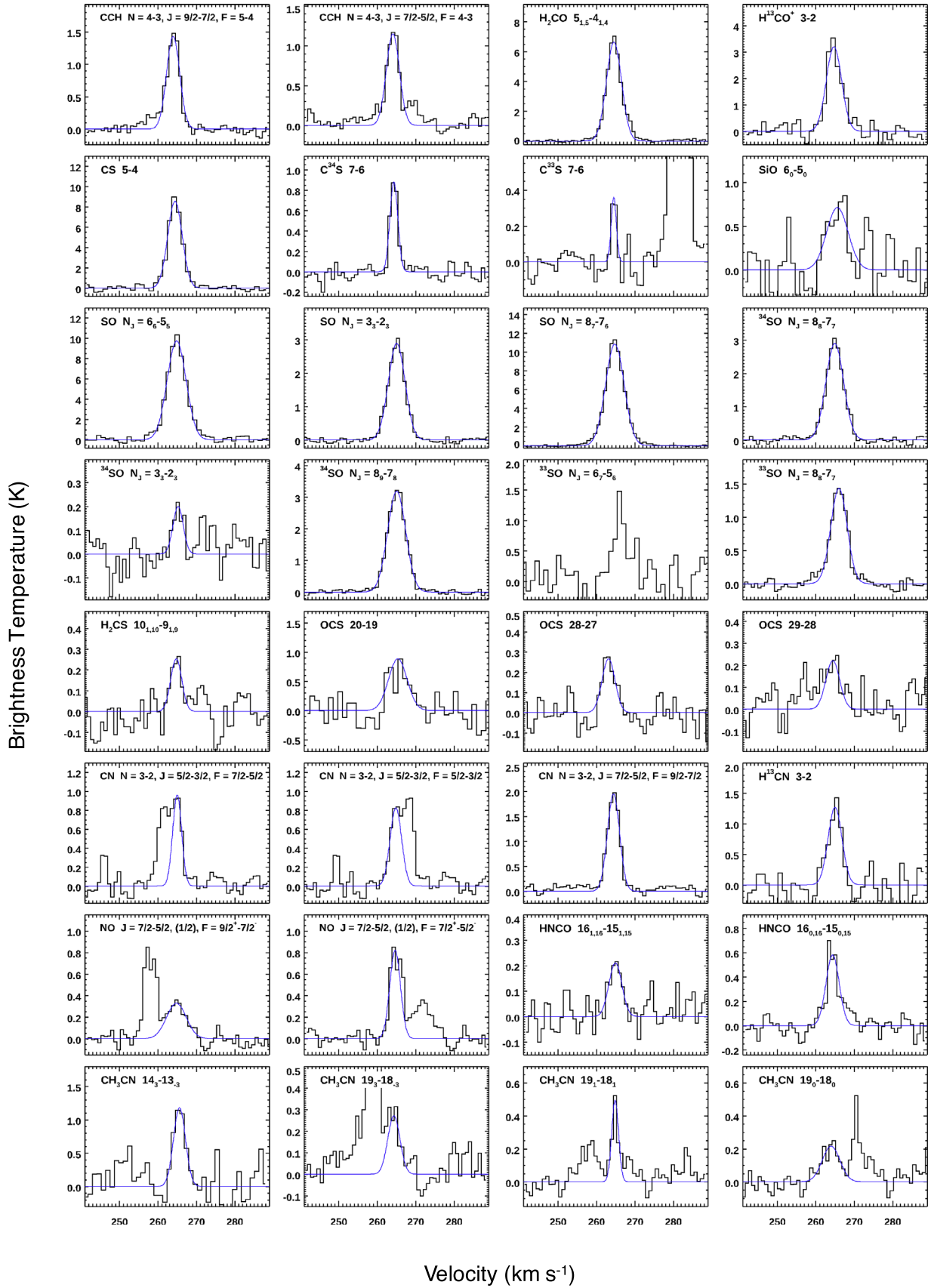


**Figure 12.** ALMA spectra of CS, SO, H<sup>13</sup>CO<sup>+</sup>, OCS, <sup>33</sup>SO, H<sup>13</sup>CN, SiO, and CH<sub>3</sub>CN lines extracted from the 0''/45 diameter region centered at ST16. The blue lines represent Gaussian profiles fitted to the spectra. For the <sup>33</sup>SO line, the integrated intensities are derived by directly integrating the spectra between 259.0 and 269.5 km s<sup>-1</sup> (see Section 3.1 for more details).

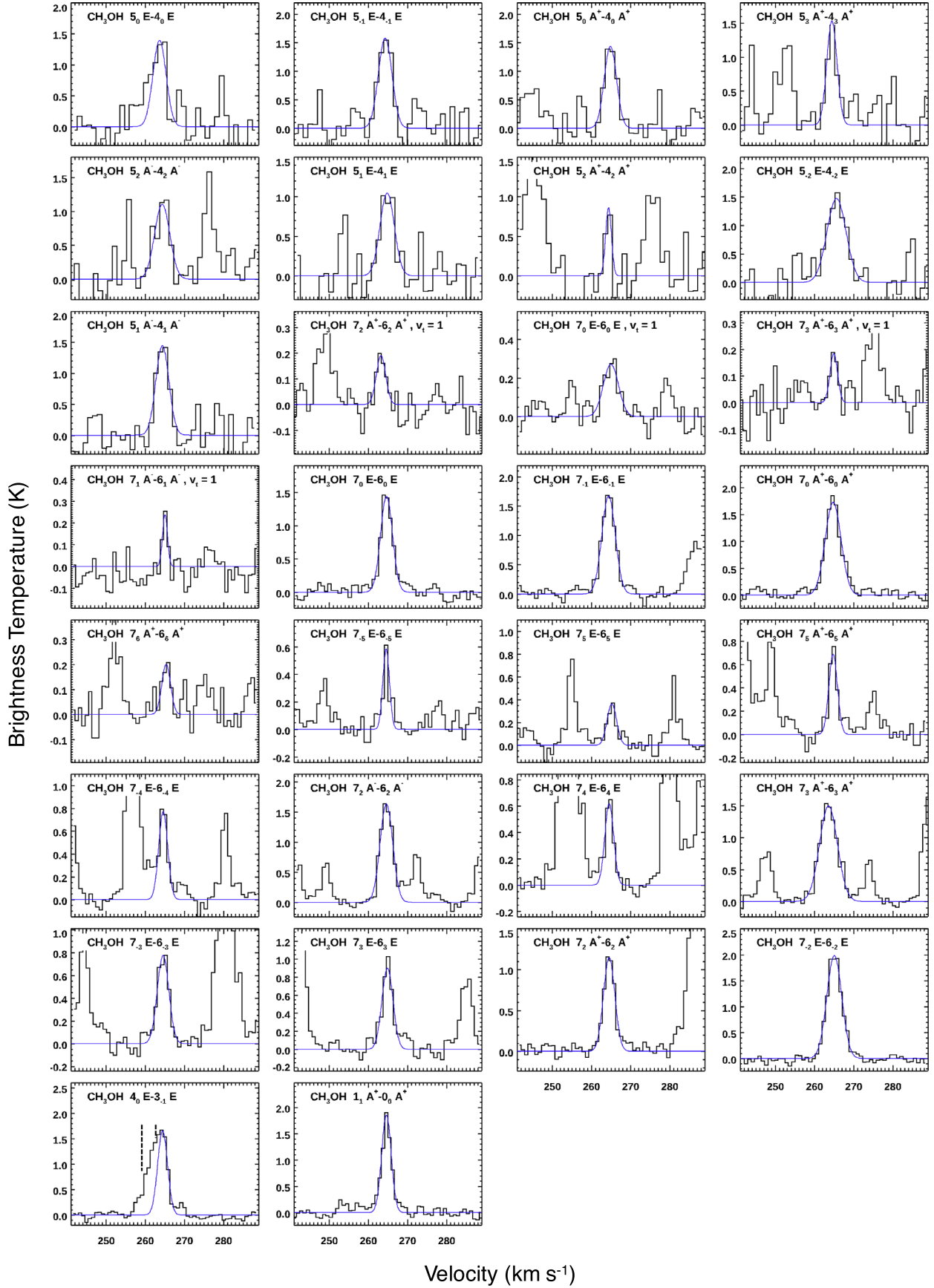


**Figure 13.** ALMA spectra of  $\text{CH}_3\text{OH}$  emission lines as in Figure 12. The spectra are sorted in ascending order of upper state energy (the emission line with the lowest upper state energy is shown in the upper left panel and that with the highest energy is in the lower right panel).



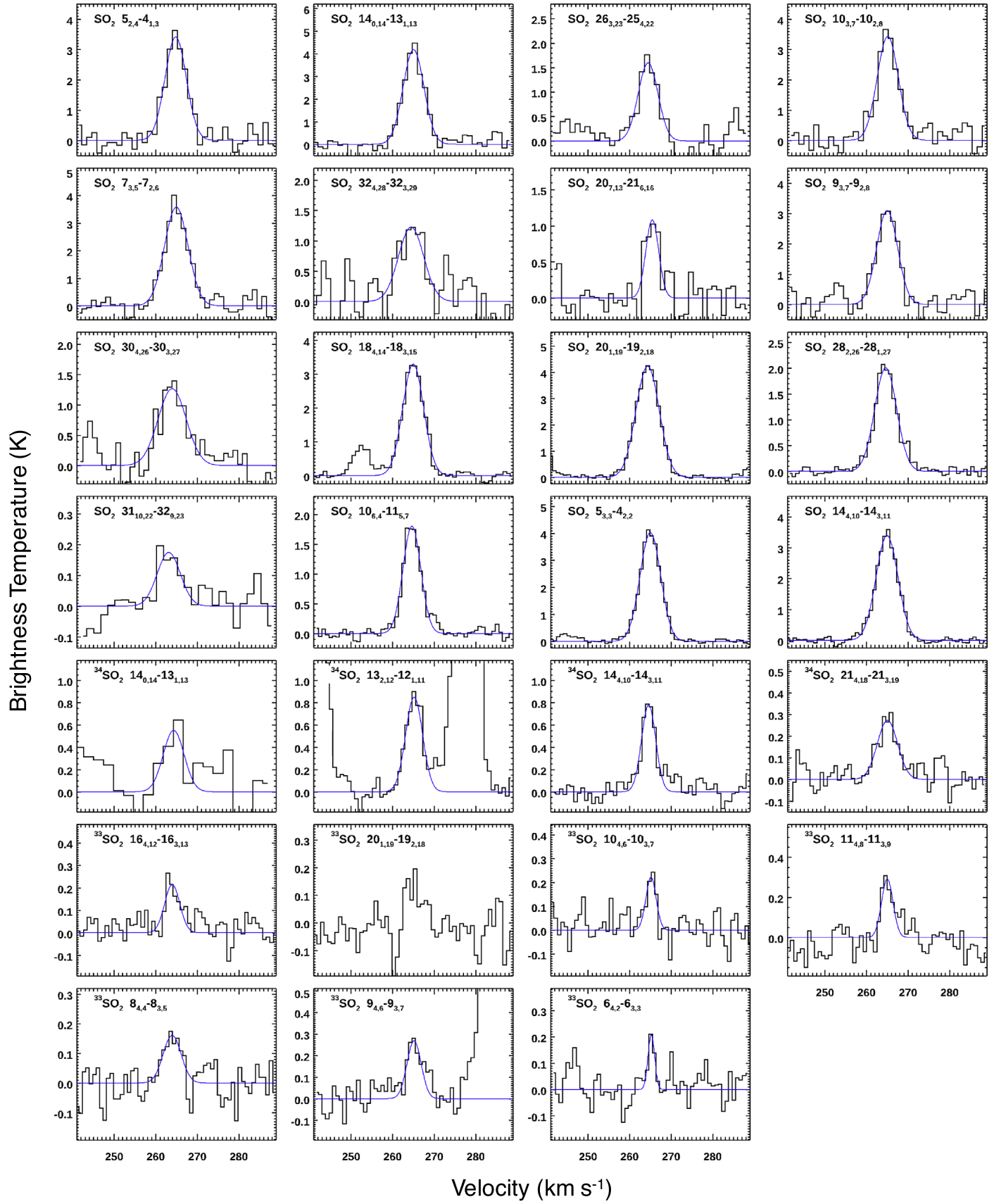


**Figure 14.** ALMA spectra of  $\text{SO}_2$  emission lines as in Figure 12. The spectra are sorted in ascending order of upper state energy (the emission line with the lowest upper state energy is shown in the upper left panel and that with the highest energy is in the lower right panel).

## Appendix C

### Details of the Astrochemical Simulations

The present astrochemical simulations use a gas-grain chemical network code that is previously adopted in, e.g., Gorai et al. (2017) and Sil et al. (2018). We have assumed that the gas and grains are coupled through accretion and various desorption mechanisms, including thermal, nonthermal (Garrod & Herbst 2006), and cosmic-ray desorption processes. The present gas-phase chemical network is based on the UMIST 2012 database (McElroy et al. 2013), while the grain surface network is mainly based on Hasegawa et al. (1992) and Ruaud et al. (2016).

For physical conditions, we have considered three different successive evolutionary stages (i.e., cold, warm-up, and post-warm-up) as employed in, e.g., Garrod (2013). The warm-up and post-warm-up stages correspond to the hot core. Important parameters used in the simulations are summarized in Table 10. Initial elemental abundances for the LMC and Galactic cases are taken from the low-metal abundance model presented in Acharyya & Herbst (2015). Details of each evolutionary stages are described below.

The first stage is a quiescent molecular cloud, where the cold gas chemistry and the ice mantle formation occur. At this stage, we consider a static molecular cloud with a gas density of  $n_{\text{H}} = 2 \times 10^4 \text{ cm}^{-3}$ . Grain surface chemistry is sensitive to the dust temperature and has a considerable effect on the subsequent hot core chemistry. Thus, visual extinction values ( $A_V$ ) are varied from 1 to 5 mag in order to investigate the effect of initial physical conditions on the hot core chemistry. The cold stage continues up to  $10^5 \text{ yr}$ .

Dust temperatures are related to  $A_V$  and the interstellar radiation field strength using the following equation as presented in Hocuk et al. (2017):

$$T_{\text{d}}^{\text{Hoc}} = [11 + 5.7 \tanh(0.61 - \log_{10}(A_V \cdot Z))] \chi_{\text{uv}}^{1/5.9}, \quad (5)$$

where  $\chi_{\text{uv}}$  is the Draine UV field strength (Draine 1978), corresponding to  $1.7 G_0$  using the Habing field (Habing 1968). In the above equation, we have scaled down  $A_V$  by the metallicity factor ( $Z$ ), which is introduced here to mimic the metallicity effect. We here consider a metallicity factor of one-third for the LMC simulations. Note that  $A_V = 1 \text{ mag}$  (MW) and one-third mag (LMC) correspond to the gas column density of  $N_{\text{H}_2} = 2.8 \times 10^{21} \text{ cm}^{-2}$  using the  $N_{\text{H}_2}/A_V$  conversion factor described in Section 4.3.2. The average interstellar radiation field strength in the LMC is suggested to be several times higher compared to the solar neighborhood based on the SED modeling of dust emission from the LMC (e.g., Meixner et al. 2010; Galliano et al. 2011). We here use a three times higher  $\chi_{\text{uv}}$  value for the LMC case.

A warm-up and collapsing stage, where the sublimation of ices occurs, follows the quiescent stage subsequently. At this stage, the gas density and the visual extinction gradually increase up to  $n_{\text{H}} = 6 \times 10^6 \text{ cm}^{-3}$  and 100 mag to be consistent with the observational constraints of the ST16 hot core, as discussed in Section 4.3.4. The temperature gradually increases up to  $T_{\text{max}} = 150 \text{ K}$ , which roughly corresponds to the observed rotation temperature of the hot molecular gas ( $\text{CH}_3\text{OH}$  and  $\text{SO}_2$ , see Section 4.1). The warm-up stage continues up to  $t_{\text{h}} = 5 \times 10^4 \text{ yr}$  in our model.

The final stage is a post-warm-up period, which will start just after the warm-up stage and the high-temperature chemistry

Table 10

Summary of the Physical Parameters Used in the Astrochemical Simulations

Grain size	0.1 $\mu\text{m}$
Surface site density	$1.5 \times 10^{15} \text{ cm}^{-2}$
Gas to dust ratio	100 (MW), 300 (LMC)
Reactive desorption factor	0.01
Ratio of the diffusion energy to the desorption energy	0.5
Interstellar UV radiation field ( $\chi_{\text{uv}}$ )	1 (MW), 3 (LMC)
Metallicity factor ( $Z$ )	1 (MW), 1/3 (LMC)
Sticking coefficient	0.5
Cosmic-ray ionization rate	$1.3 \times 10^{-17} \text{ s}^{-1}$
Initial hydrogen number density	$2 \times 10^4 \text{ cm}^{-3}$
Final hydrogen number density	$6 \times 10^6 \text{ cm}^{-3}$
Cold stage (1st phase)	$10^5 \text{ yr}$
Warm-up and collapsing stage (2nd phase)	$5 \times 10^4 \text{ yr}$
Post-warm-up stage (3rd phase)	$1.0 \times 10^5 \text{ yr}$
Initial $A_V$	1–5 mag
Final $A_V$	100 mag
$T_{\text{max}}$	150 K

proceeds. The post-warm-up stage continues up to  $10^5 \text{ yr}$ , in which the density and temperature remain the same as they were in the last phase of the warm-up stage. Adding up the above three stages, the total simulation time in our astrochemical model is  $t_{\text{tot}} = 2.5 \times 10^5 \text{ yr}$ .

## ORCID iDs

Takashi Shimonishi  <https://orcid.org/0000-0002-0095-3624>  
 Ankan Das  <https://orcid.org/0000-0003-4615-602X>  
 Nami Sakai  <https://orcid.org/0000-0002-3297-4497>  
 Kei E. I. Tanaka  <https://orcid.org/0000-0002-6907-0926>  
 Yuri Aikawa  <https://orcid.org/0000-0003-3283-6884>  
 Takashi Onaka  <https://orcid.org/0000-0002-8234-6747>  
 Yoshimasa Watanabe  <https://orcid.org/0000-0002-9668-3592>  
 Yuri Nishimura  <https://orcid.org/0000-0003-0563-067X>

## References

- Acharyya, K., & Herbst, E. 2015, *ApJ*, **812**, 142  
 Acharyya, K., & Herbst, E. 2018, *ApJ*, **859**, 51  
 Anderson, C. N., Meier, D. S., Ott, J., et al. 2014, *ApJ*, **793**, 37  
 Andrievsky, S. M., Kovtyukh, V. V., Korotin, S. A., Spite, M., & Spite, F. 2001, *A&A*, **367**, 605  
 Balucani, N., Ceccarelli, C., & Taquet, V. 2015, *MNRAS*, **449**, L16  
 Bayet, E., Viti, S., Williams, D. A., & Rawlings, J. M. C. 2008, *ApJ*, **676**, 978  
 Beltrán, M. T., Cesaroni, R., Neri, R., & Codella, C. 2011a, *A&A*, **525**, A151  
 Beltrán, M. T., Cesaroni, R., Zhang, Q., et al. 2011b, *A&A*, **532**, A91  
 Beuther, H., Zhang, Q., Bergin, E. A., et al. 2007, *A&A*, **468**, 1045  
 Bisschop, S. E., Jørgensen, J. K., van Dishoeck, E. F., & de Wachter, E. B. M. 2007, *A&A*, **465**, 913  
 Blake, G. A., Sutton, E. C., Masson, C. R., & Phillips, T. G. 1987, *ApJ*, **315**, 621  
 Boogert, A. C. A., Huard, T. L., Cook, A. M., et al. 2011, *ApJ*, **729**, 92  
 Charnley, S. B. 1997, *ApJ*, **481**, 396  
 Chin, Y.-N., Henkel, C., Whiteoak, J. B., Langer, N., & Churchwell, E. B. 1996, *A&A*, **305**, 960  
 Chin, Y.-N., Henkel, C., Whiteoak, J. B., et al. 1997, *A&A*, **317**, 548  
 Cox, A. N. 2000, *Allen's Astrophysical Quantities* (Berlin: Springer)  
 Draine, B. T. 1978, *ApJS*, **36**, 595  
 Dufour, R. J., Shields, G. A., & Talbot, R. J., Jr. 1982, *ApJ*, **252**, 461  
 Fitzpatrick, E. L. 1985, *ApJ*, **299**, 219  
 Fuente, A., Martín-Pintado, J., Cernicharo, J., & Bachiller, R. 1993, *A&A*, **276**, 473  
 Fukui, Y., Harada, R., Tokuda, K., et al. 2015, *ApJL*, **807**, L4  
 Furuya, R. S., Cesaroni, R., & Shinnaga, H. 2011, *A&A*, **525**, A72

- Galliano, F., Hony, S., Bernard, J. P., et al. 2011, *A&A*, **536**, A88
- Garrod, R. T. 2013, *ApJ*, **765**, 60
- Garrod, R. T., & Herbst, E. 2006, *A&A*, **457**, 927
- Gerner, T., Beuther, H., Semenov, D., et al. 2014, *A&A*, **563**, A97
- Goldsmith, P. F., & Langer, W. D. 1999, *ApJ*, **517**, 209
- Gorai, P., Das, A., Das, A., et al. 2017, *ApJ*, **836**, 70
- Habing, H. J. 1968, *BAN*, **19**, 421
- Hasegawa, T. I., Herbst, E., & Leung, C. M. 1992, *ApJS*, **82**, 167
- Heikkilä, A., Johansson, L. E. B., & Olofsson, H. 1999, *A&A*, **344**, 817
- Helmich, F. P., & van Dishoeck, E. F. 1997, *A&AS*, **124**, 205
- Herbst, E., & Klemperer, W. 1973, *ApJ*, **185**, 505
- Herbst, E., & van Dishoeck, E. F. 2009, *ARA&A*, **47**, 427
- Hocuk, S., Szűcs, L., Caselli, P., et al. 2017, *A&A*, **604**, A58
- Hosokawa, T., & Omukai, K. 2009, *ApJ*, **703**, 1810
- Indebetouw, R., Brogan, C., Chen, C.-H. R., et al. 2013, *ApJ*, **774**, 73
- Jansen, D. J., Spaans, M., Hogerheijde, M. R., & van Dishoeck, E. F. 1995, *A&A*, **303**, 541
- Johansson, L. E. B., Olofsson, H., Hjalmarson, A., Gredel, R., & Black, J. H. 1994, *A&A*, **291**, 89
- Kato, D., Nagashima, C., Nagayama, T., et al. 2007, *PASJ*, **59**, 615
- Kemper, F., Woods, P. M., Antoniou, V., et al. 2010, *PASP*, **122**, 683
- Kobayashi, C., Karakas, A. I., & Umeda, H. 2011, *MNRAS*, **414**, 3231
- Koornneef, J. 1982, *A&A*, **107**, 247
- Kurtz, S., Cesaroni, R., Churchwell, E., Hofner, P., & Walmsley, C. M. 2000, in *Protostars and Planets IV*, ed. V. Mannings, A. P. Boss, & S. S. Russell (Tucson, AZ: Univ. Arizona Press), 299
- McElroy, D., Walsh, C., Markwick, A. J., et al. 2013, *A&A*, **550**, A36
- McKee, C. F., & Tan, J. C. 2003, *ApJ*, **585**, 850
- Meixner, M., Galliano, F., Hony, S., et al. 2010, *A&A*, **518**, L71
- Meixner, M., Gordon, K. D., Indebetouw, R., et al. 2006, *AJ*, **132**, 2268
- Meixner, M., Panuzzo, P., Roman-Duval, J., et al. 2013, *AJ*, **146**, 62
- Müller, H. S. P., Schlöder, F., Stutzki, J., & Winnewisser, G. 2005, *JMoSt*, **742**, 215
- Müller, H. S. P., Thorwirth, S., Roth, D. A., & Winnewisser, G. 2001, *A&A*, **370**, L49
- Nayak, O., Meixner, M., Fukui, Y., et al. 2018, *ApJ*, **854**, 154
- Nishimura, Y., Shimonishi, T., Watanabe, Y., et al. 2016, *ApJ*, **829**, 94
- Nomura, H., & Millar, T. J. 2004, *A&A*, **414**, 409
- Oliveira, J. M., van Loon, J. T., Chen, C., et al. 2009, *ApJ*, **707**, 1269
- Oliveira, J. M., van Loon, J. T., Sloan, G. C., et al. 2011, *MNRAS*, **411**, L36
- Ossenkopf, V., & Henning, T. 1994, *A&A*, **291**, 943
- Paron, S., Ortega, M. E., Cunningham, M., et al. 2014, *A&A*, **572**, A56
- Paron, S., Ortega, M. E., Fariña, C., et al. 2016, *MNRAS*, **455**, 518
- Pauly, T., & Garrod, R. T. 2018, *ApJ*, **854**, 13
- Pety, J., Guzmán, V. V., Orkisz, J. H., et al. 2017, *A&A*, **599**, A98
- Pickett, H. M., Poynter, R. L., Cohen, E. A., et al. 1998, *JQSRT*, **60**, 883
- Pietrzyński, G., Graczyk, D., Gieren, W., et al. 2013, *Natur*, **495**, 76
- Pineau des Forets, G., Roueff, E., & Flower, D. R. 1990, *MNRAS*, **244**, 668
- Robitaille, T. P., Whitney, B. A., Indebetouw, R., & Wood, K. 2007, *ApJS*, **169**, 328
- Rodriguez-Franco, A., Martin-Pintado, J., & Fuente, A. 1998, *A&A*, **329**, 1097
- Rolleston, W. R. J., Trundle, C., & Dufton, P. L. 2002, *A&A*, **396**, 53
- Ruud, M., Wakelam, V., & Hersant, F. 2016, *MNRAS*, **459**, 3756
- Russell, S. C., & Dopita, M. A. 1992, *ApJ*, **384**, 508
- Saigo, K., Onishi, T., Nayak, O., et al. 2017, *ApJ*, **835**, 108
- Schilke, P., Groesbeck, T. D., Blake, G. A., & Phillips, T. G. 1997, *ApJS*, **108**, 301
- Seale, J. P., Looney, L. W., Chen, C.-H. R., Chu, Y.-H., & Gruendl, R. A. 2011, *ApJ*, **727**, 36
- Seale, J. P., Looney, L. W., Chu, Y., et al. 2009, *ApJ*, **699**, 150
- Seale, J. P., Looney, L. W., Wong, T., et al. 2012, *ApJ*, **751**, 42
- Sewilo, M., Indebetouw, R., Charnley, S. B., et al. 2018, *ApJL*, **853**, L19
- Shimonishi, T., Dartois, E., Onaka, T., & Boulanger, F. 2016a, *A&A*, **585**, A107
- Shimonishi, T., Nakatani, N., Furuya, K., & Hama, T. 2018a, *ApJ*, **855**, 27
- Shimonishi, T., Onaka, T., Kato, D., et al. 2008, *ApJL*, **686**, L99
- Shimonishi, T., Onaka, T., Kato, D., et al. 2010, *A&A*, **514**, A12
- Shimonishi, T., Onaka, T., Kawamura, A., & Aikawa, Y. 2016b, *ApJ*, **827**, 72
- Shimonishi, T., Watanabe, Y., Nishimura, Y., et al. 2018b, *ApJ*, **862**, 102
- Sil, M., Gorai, P., Das, A., et al. 2018, *ApJ*, **853**, 139
- Sutton, E. C., Peng, R., Danchi, W. C., et al. 1995, *ApJS*, **97**, 455
- Tanaka, K. E. I., Tan, J. C., Zhang, Y., & Hosokawa, T. 2018, *ApJ*, **861**, 68
- Tang, X. D., Henkel, C., Chen, C.-H. R., et al. 2017, *A&A*, **600**, A16
- Turner, B. E. 1991, *ApJS*, **76**, 617
- van der Tak, F. F. S. 2004, in *IAU Symp. 221, Star Formation at High Angular Resolution*, ed. M. G. Burton, R. Jayawardhana, & T. L. Bourke (San Francisco, CA: ASP), 59
- van der Tak, F. F. S., Black, J. H., Schöier, F. L., Jansen, D. J., & van Dishoeck, E. F. 2007, *A&A*, **468**, 627
- van der Tak, F. F. S., van Dishoeck, E. F., & Caselli, P. 2000, *A&A*, **361**, 327
- van Dishoeck, E. F., & Blake, G. A. 1998, *ARA&A*, **36**, 317
- van Loon, J. T., Oliveira, J. M., Wood, P. R., et al. 2005, *MNRAS*, **364**, L71
- Vasyunin, A. I., & Herbst, E. 2013, *ApJ*, **769**, 34
- Wallström, S. H. J., Muller, S., & Guélin, M. 2016, *A&A*, **595**, A96
- Wang, M., Chin, Y.-N., Henkel, C., Whiteoak, J. B., & Cunningham, M. 2009, *ApJ*, **690**, 580
- Westerlund, B. E. 1990, *A&ARv*, **2**, 29
- Whittet, D. C. B., Gerakines, P. A., Hough, J. H., & Shenoy, S. S. 2001, *ApJ*, **547**, 872
- Wong, T., Hughes, A., Ott, J., et al. 2011, *ApJS*, **197**, 16
- Wong, T., Whiteoak, J. B., Ott, J., Chin, Y.-n., & Cunningham, M. R. 2006, *ApJ*, **649**, 224
- Zhang, Y., Higuchi, A. E., Sakai, N., et al. 2018, *ApJ*, **864**, 76
- Zhang, Y., & Tan, J. C. 2018, *ApJ*, **853**, 18
- Zhang, Y., Tan, J. C., Sakai, N., et al. 2019, *ApJ*, **873**, 73
- Ziurys, L. M., McGonagle, D., Minh, Y., & Irvine, W. M. 1991, *ApJ*, **373**, 535